Russian Research Center “ Kurchatov Institute”

Effect of Irradiation on Graphite Materials under Fusion and Fission Irradiation Conditions. Experience for the Collimators of LHC.

A.I.Ryazanov

21 March, CERN, Geneva

Technology Production of C/C Composites

Effect of Carbonization Rate:

1-1000 °C/min

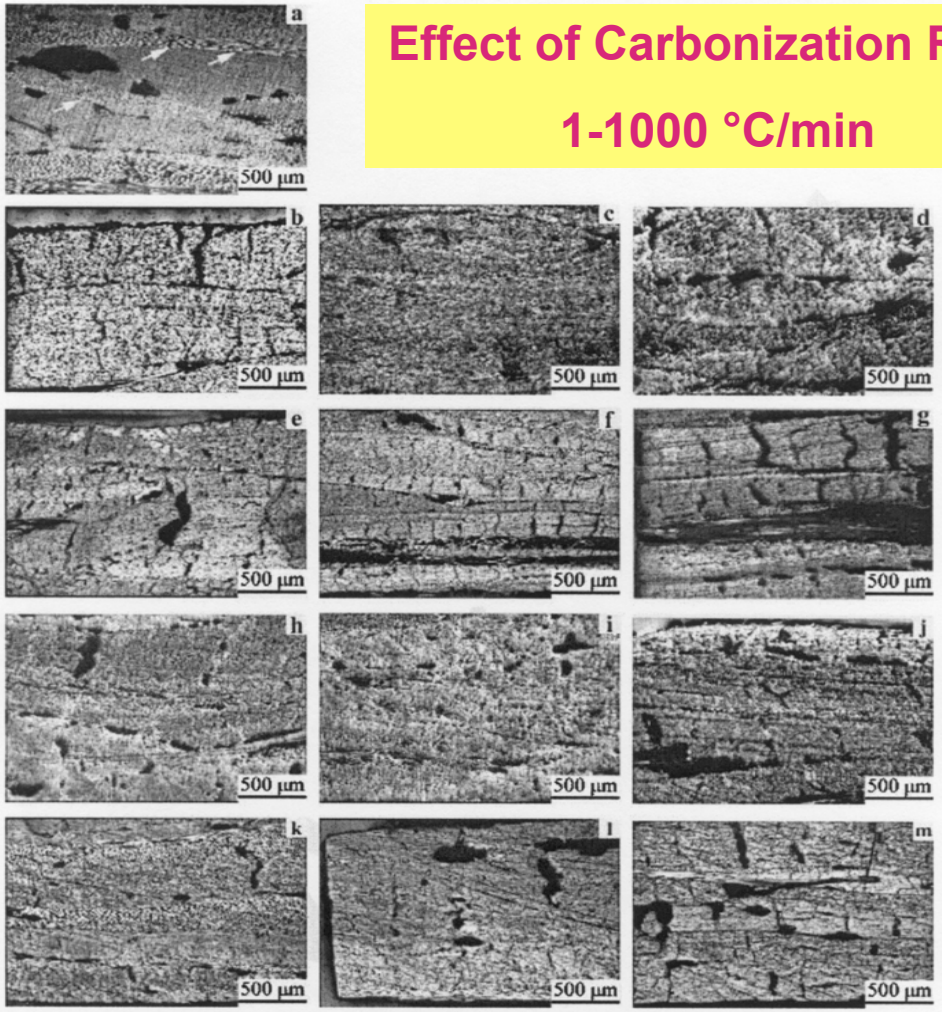

Fig. 2. Cross-sectional optical micrographs of composite under different process stages at different carbonization rates. (a) Cured, (b) C1-1, (c) C1-100, (d) C1-1000, (e) G1-1, (f) G1-100, (g) G1-1000, (h) D4-1, (i) D4-100, (j) D4-1000, (k) G2-1, (l) G2-100, (m) G2-1000.

Effect of Carbonization Rate on Porosity and Density of C/C Composites

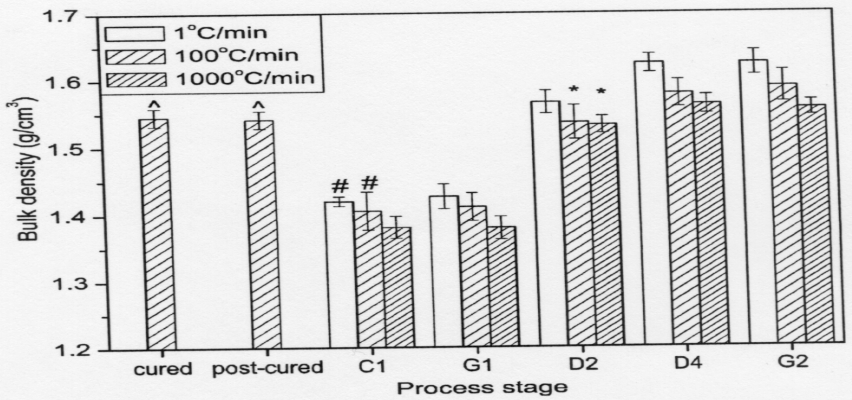

Fig. 3. Bulk densities of composite under different process stages at different carbonization rates. Same symbol indicate no statistical difference.

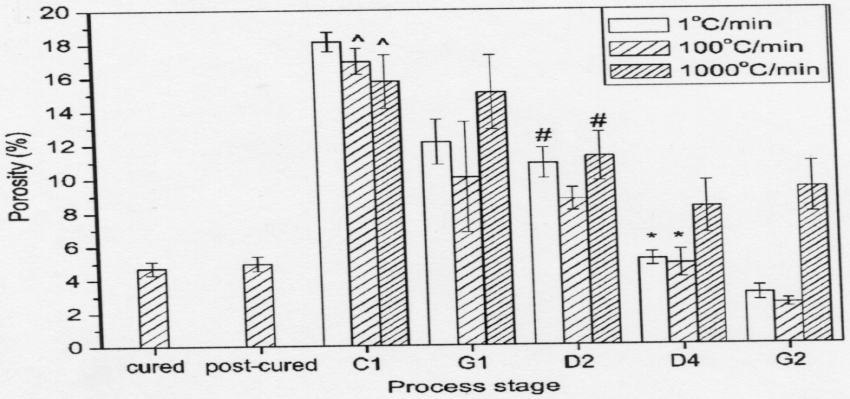

Fig. 4. Open porosity values of composite under different process stages at different carbonization rates. Same symbol indicate no statistical difference.

21 March, CERN, Geneva

Graphite materials in Tokamaks and Fusion Reactor:

- **Limiter and/or protection plate for the inner wall**

Exposition to:

- **Vacuum**
- **Intense head load**
- **Edge plasma**
- **Fast neutrons**

Important behavior:

- **Thermal shock resistance**
- **Thermo-mechanical properties**
- **Accumulation of Hydrogen and Helium in fusion reactor**
- **Accumulation of Radiation Damage**
- **Sputtering and particle emission**

Graphite materials in Atomic Reactors (RBMK):

- Reflectors and stopping system of neutrons

Exposition to:

- Temperature: T = 300-750 C
- Thermal and Fast neutrons

Important behavior:

- Radiation swelling
- Degradation of thermo-mechanical properties
- Cracking and fracture

Main differences between irradiation conditions of materials in LHC under 7 TeV proton irradiation and in atomic, fusion reactors

1. Shock waves propagation under fast neutron irradiation.
   (Cracks can form during propagation of shock wave on point defects clusters, which are created under neutron irradiation).
2. Neutron irradiation spectrum has a part of neutrons with very high energies up to 100 GeV.
   (Formation of high density of cascades and subcascades and primary radiation defects).
3. Accumulation in matrix of high concentration of hydrogen and helium atoms due to nuclear reactions.
   (Formation of hydrogen and helium bubbles, degradation of mechanical properties due to embrittlement).
4. Effect of shock waves on vacuum.

21 March, CERN, Geneva

Thermal Shocks

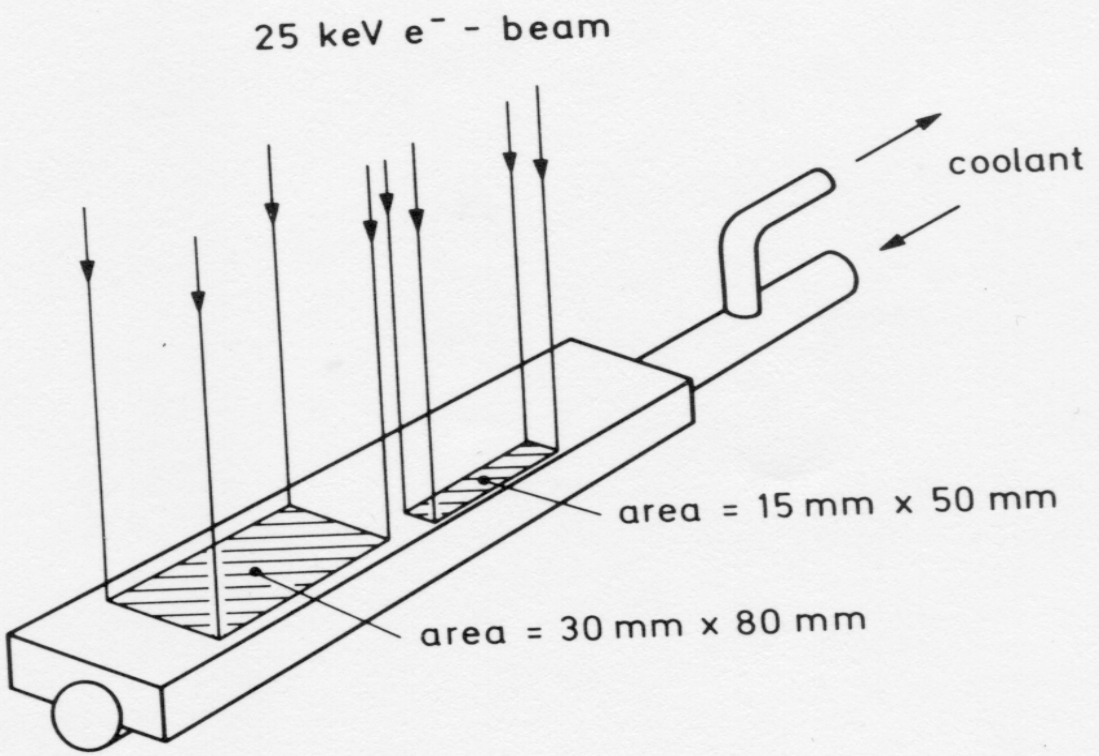

Fig. 4. Sketch of the directly cooled graphite block brazed to a Mo tube. The heated zones are indicated by the hatched areas.

Thermal Shocks

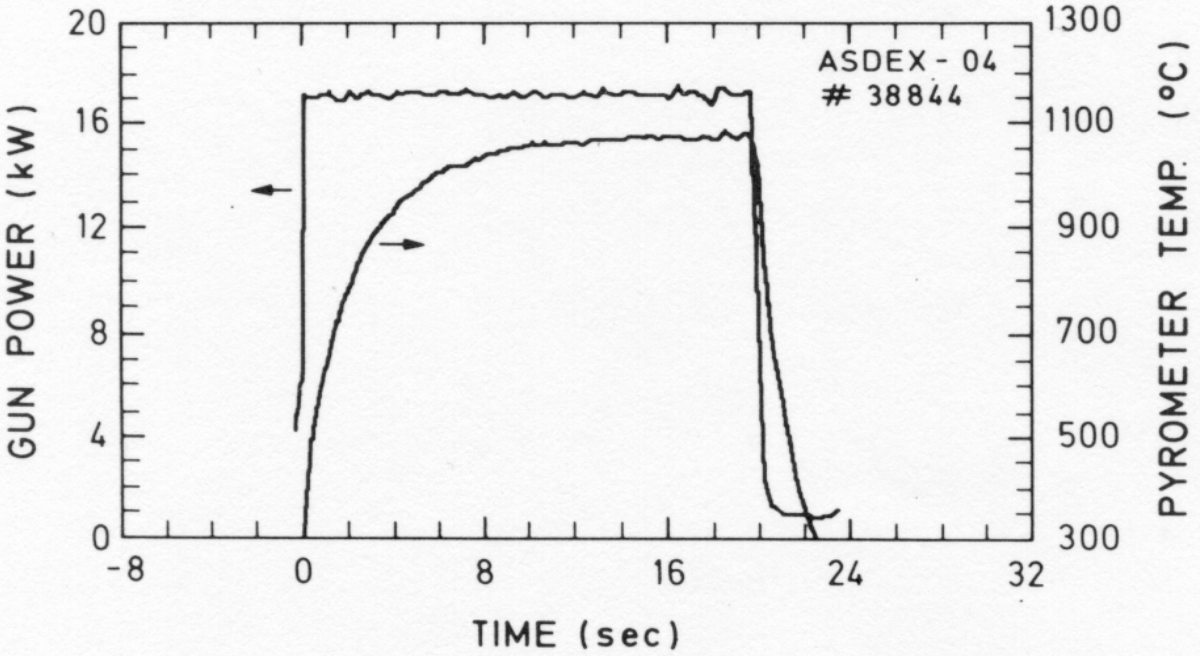

Fig. 5. Heating power and graphite surface temperature versus time.

Shocked Sample

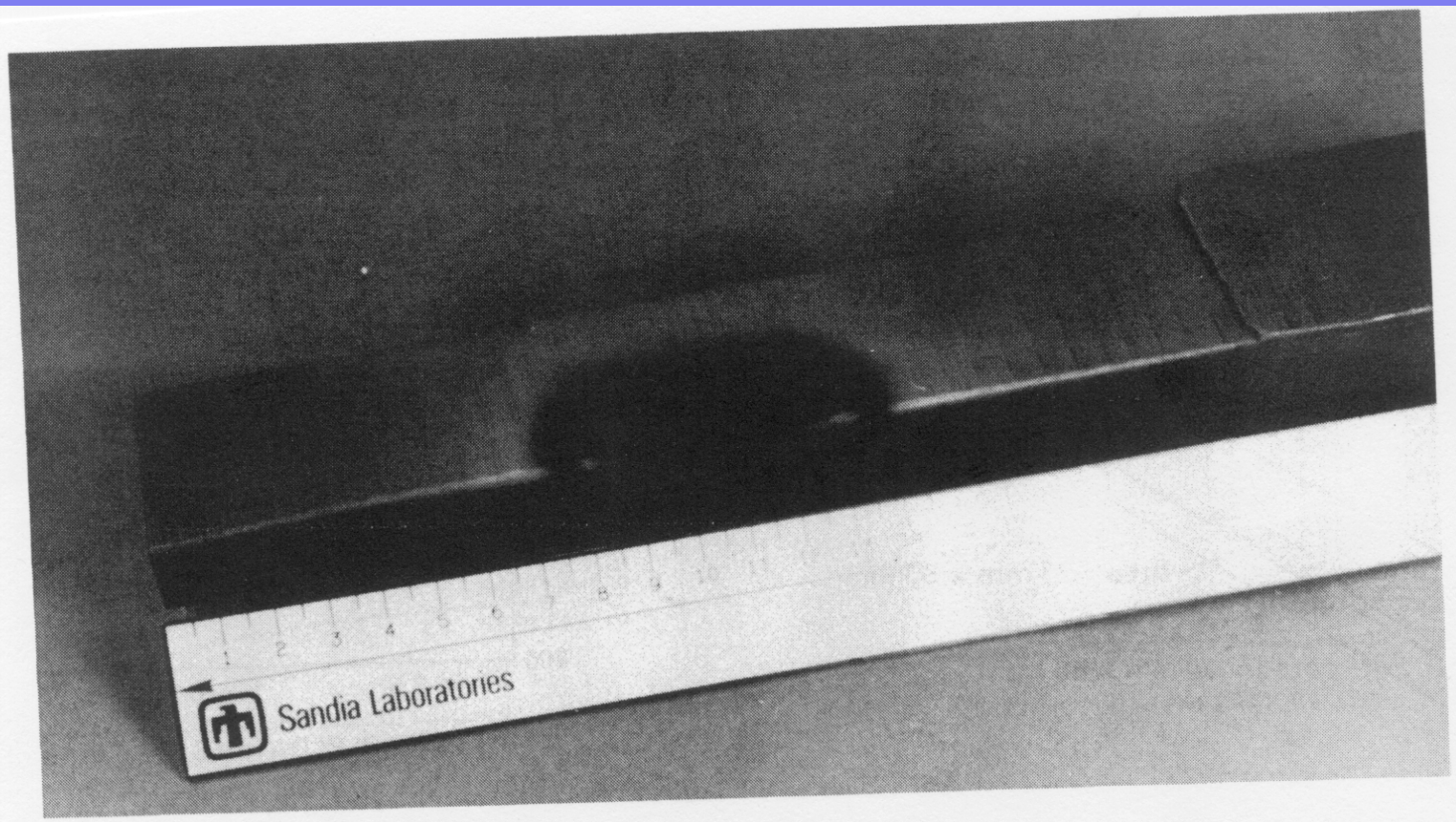

Fig. 7. The directly cooled graphite block after the high-heat-flux test. The dark area is eroded during the heat pulses.

Thermal Shock

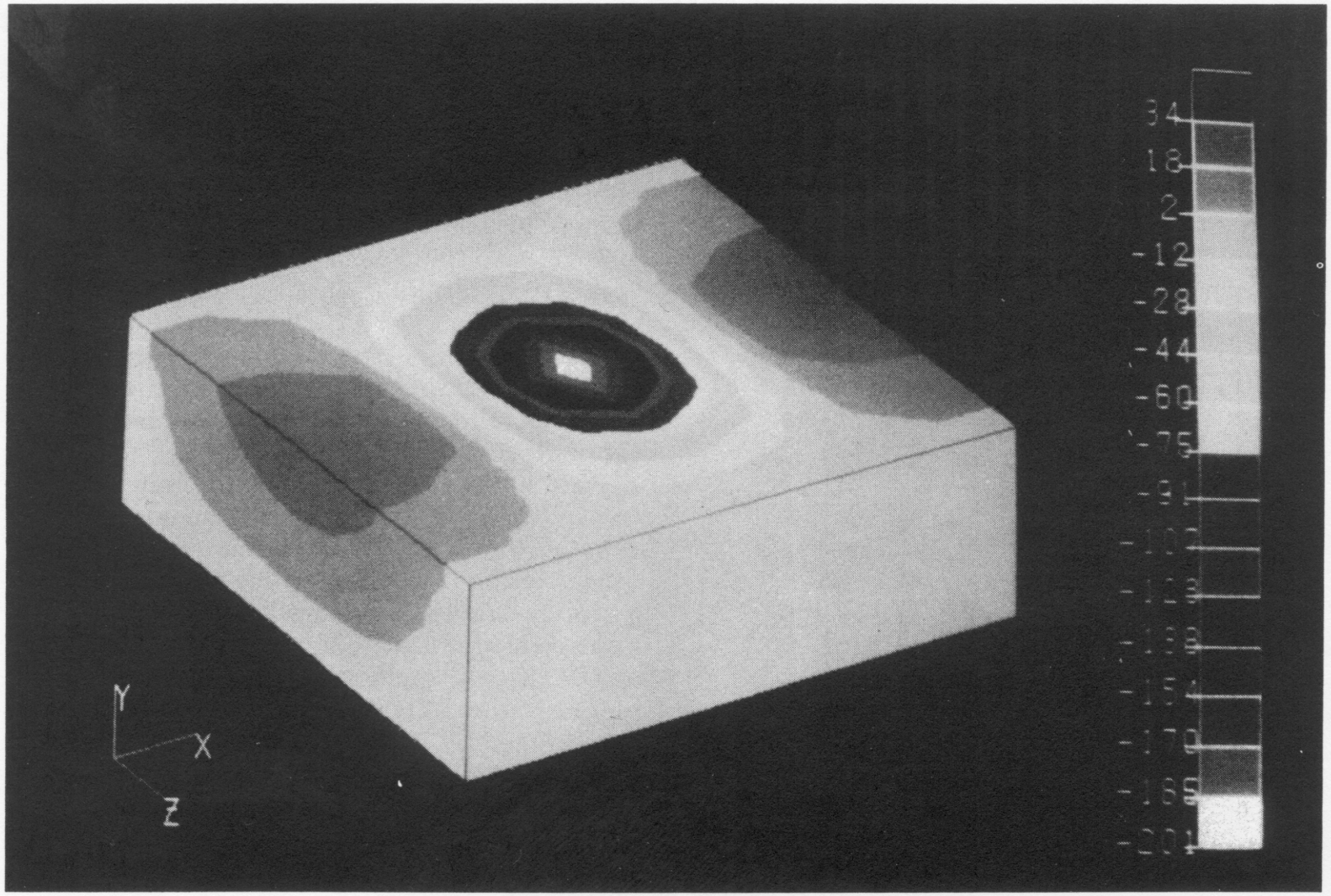

Fig. 13. Stress distribution in a heated sample.

Microstructure Change due to Shock

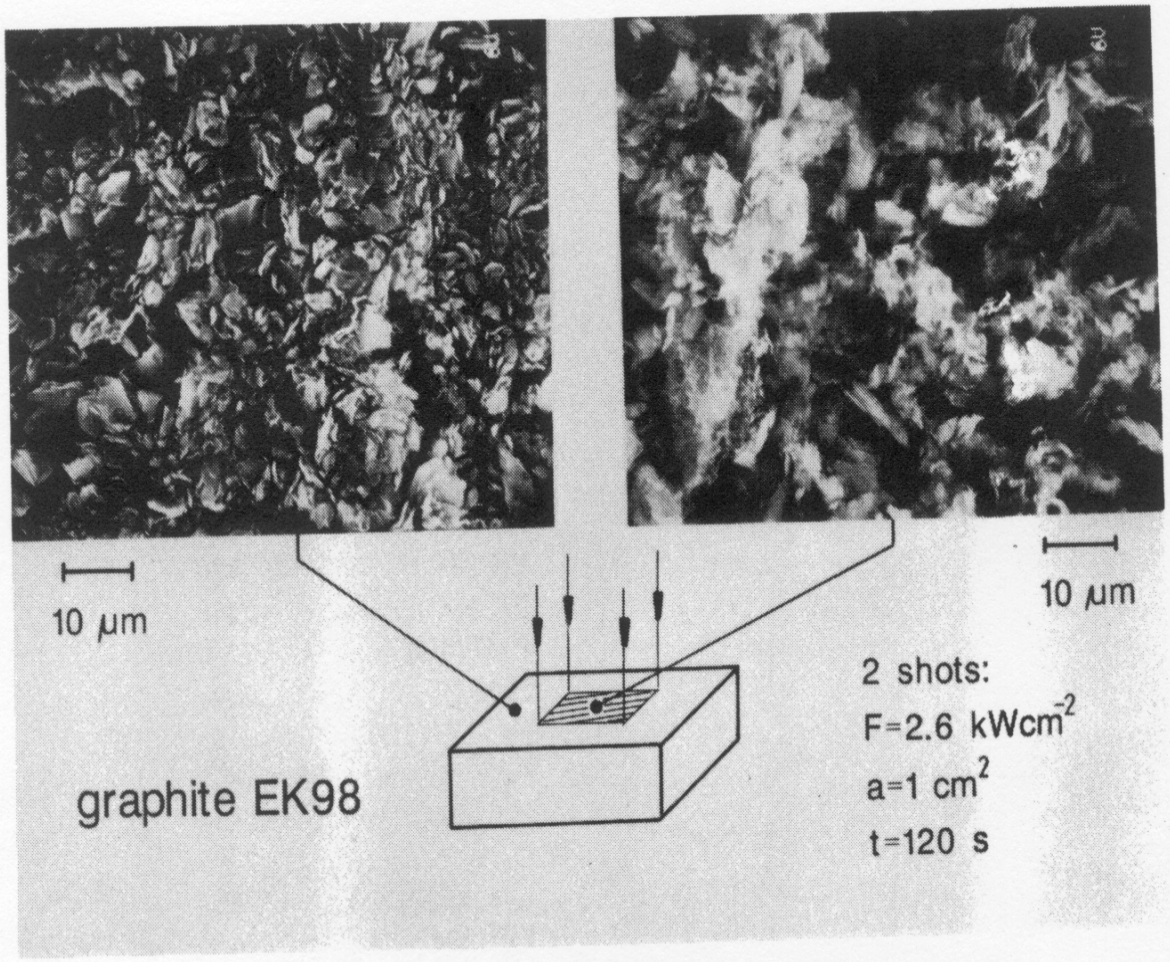

Fig. 9. An SEM image of the surface structure of a heated (right) and unheated (left) part of the sample.

Erosion due to thermal shock

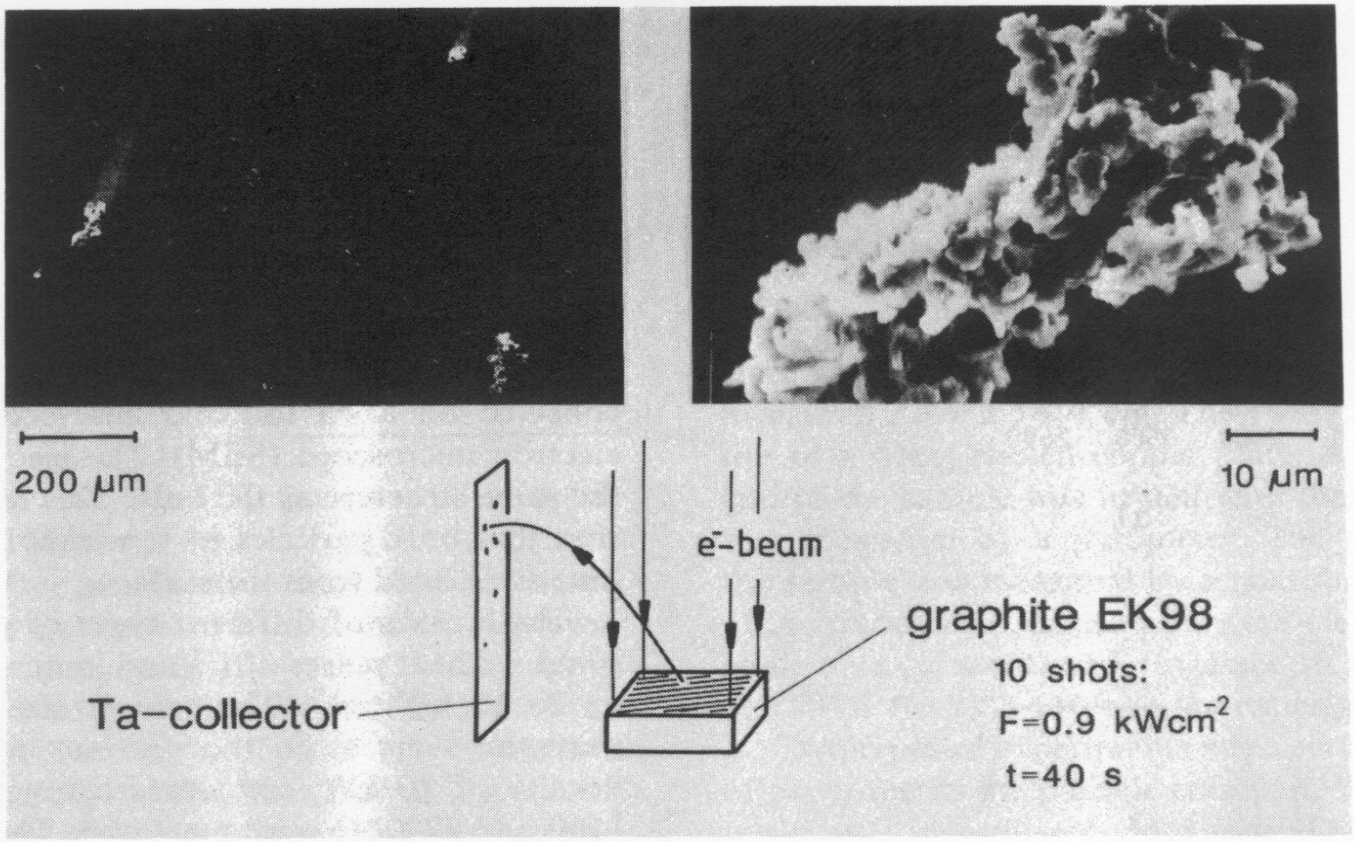

Fig. 10. Emitted graphite particles collected onto a Ta foil.

Erosion due to Thermal Shock

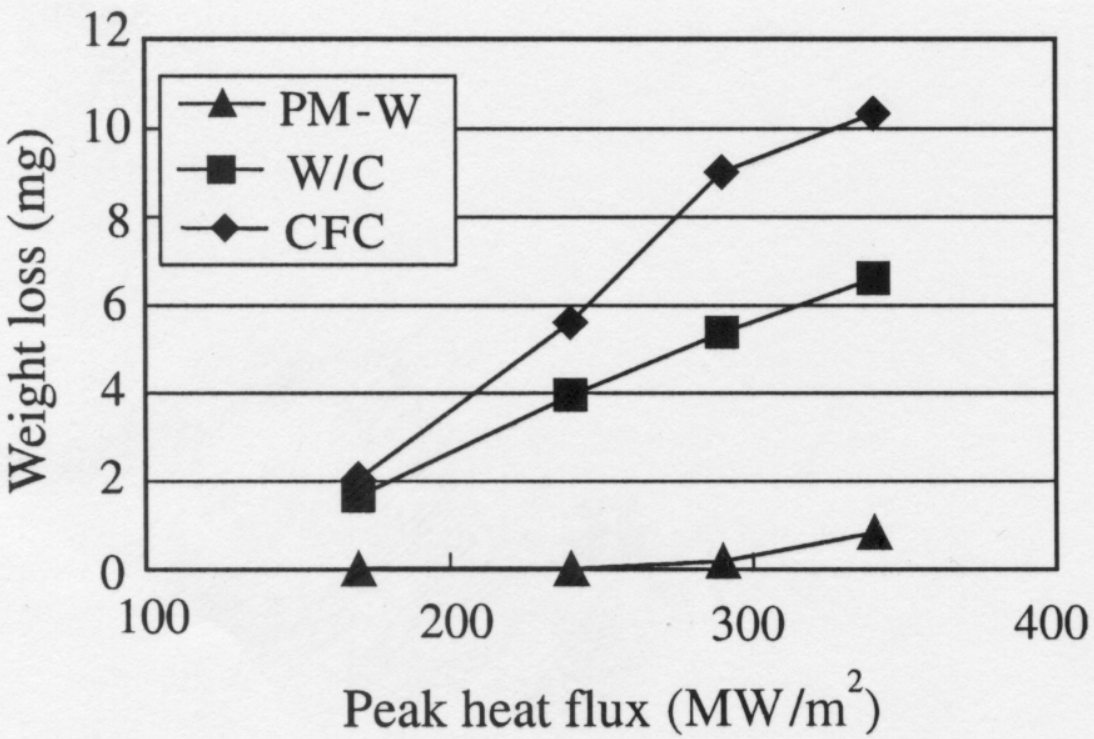

Fig. 3. Weight loss of PM-W, W/Cu coating and C/C composite versus peak heat flux.

Erosion due to Thermal Shock

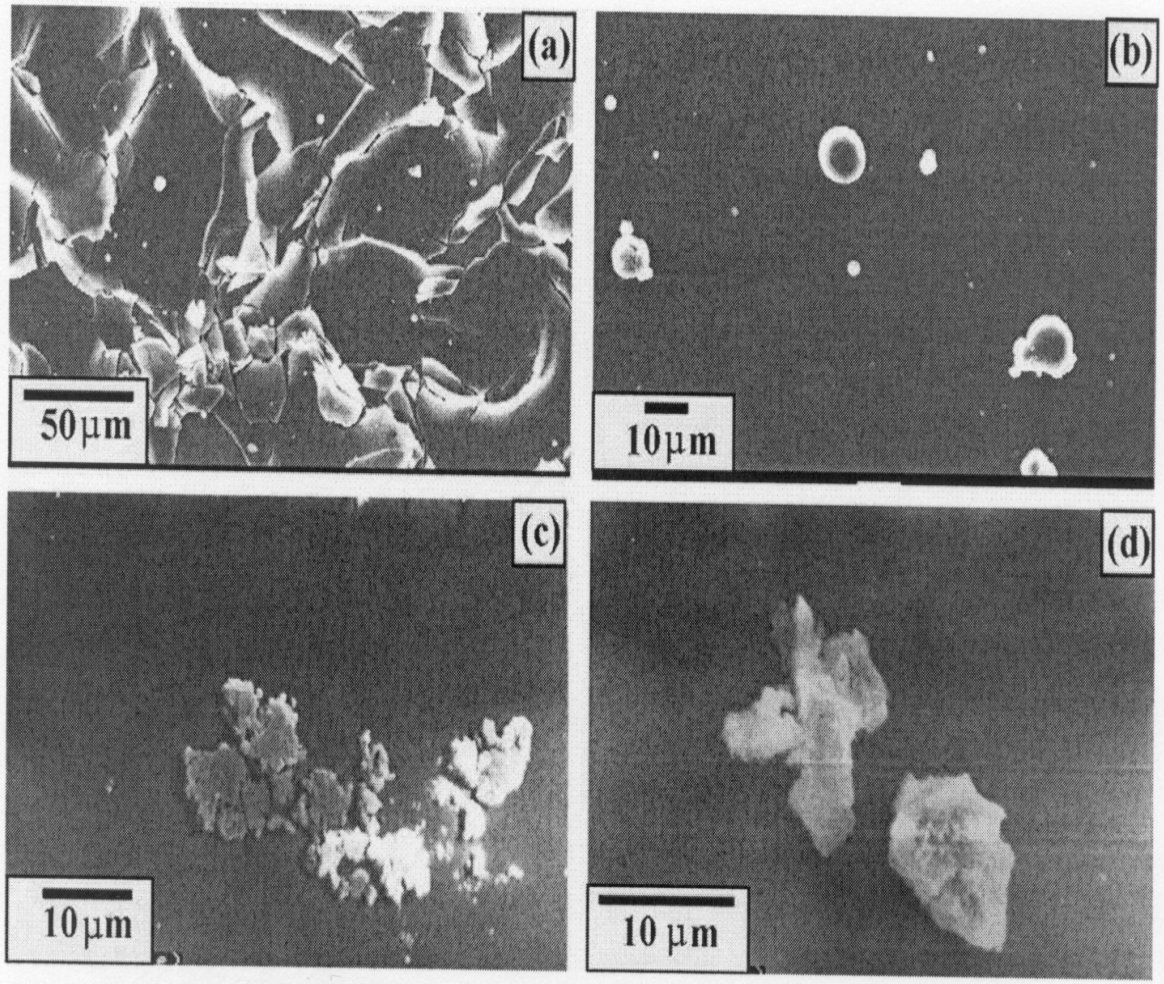

Fig. 5. SEM images of erosion products for B_4C/Cu (a) and (b), and for W/CFC (c) and (d).

Erosion due to Thermal Shock

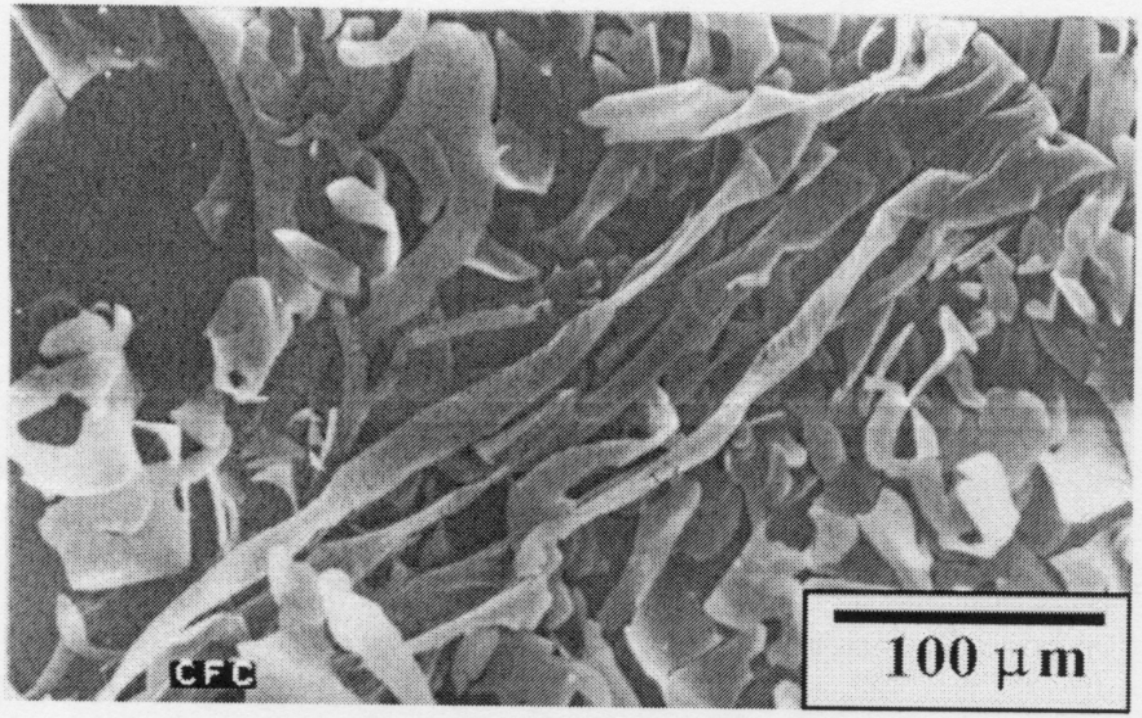

Fig. 6. Erosion products of C/C composite by a pulsed electron beam (170 MW/m^2, 1 s).

Cracking due to thermal shock

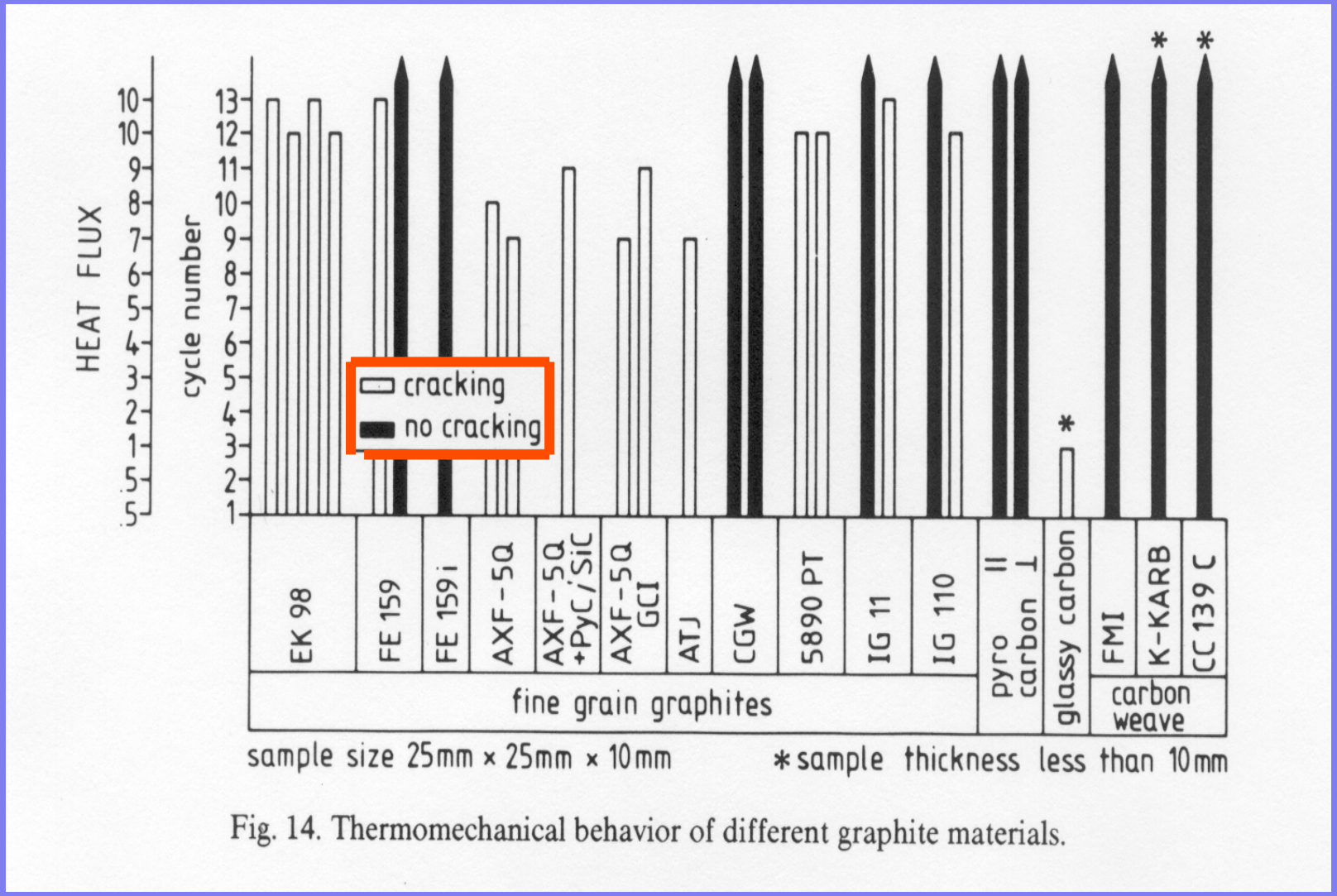

Fig. 14. Thermomechanical behavior of different graphite materials.

Microstructure Change

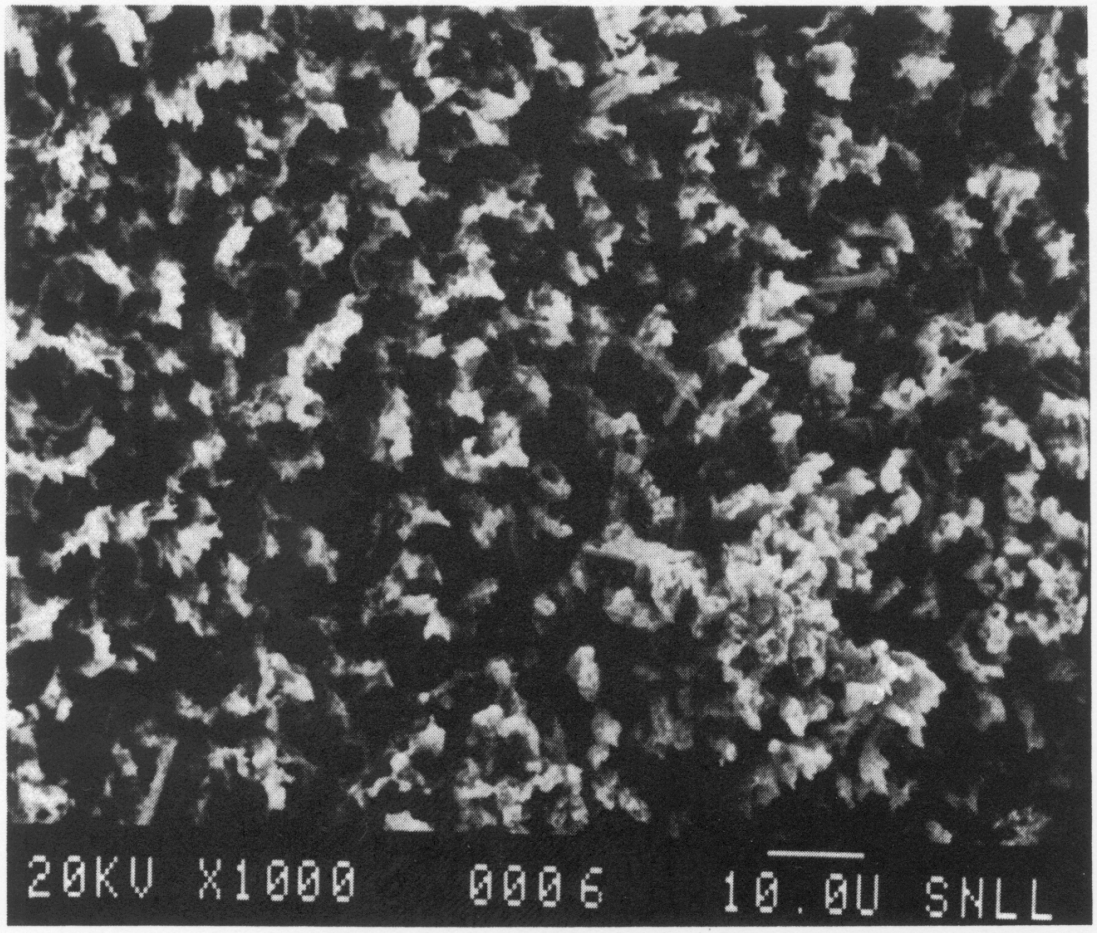

Fig. 17. An SEM image of a POCO graphite surface exposed to a H plasma in PISCES. Redeposition of C on the graphite surface is found.

Surface Modification of Graphite after Deuterium Plasma Irradiation

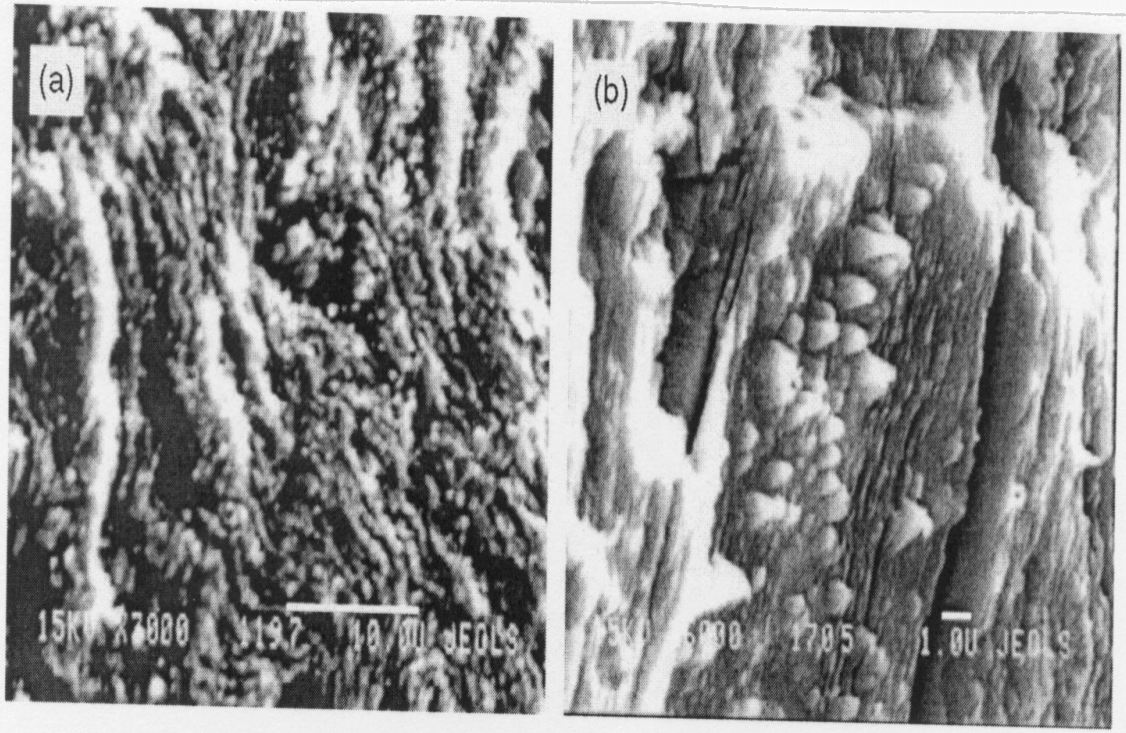

Fig. 2. Surface microstructures of MPG-8 graphite (a) and SEP NB31 composite (b) after deuterium plasma irradiation (5 eV, 10^{26} m^{-2}) at 1470 K (MPG-8) and at 1320 K (SEP NB31).

Thermal Shock Load

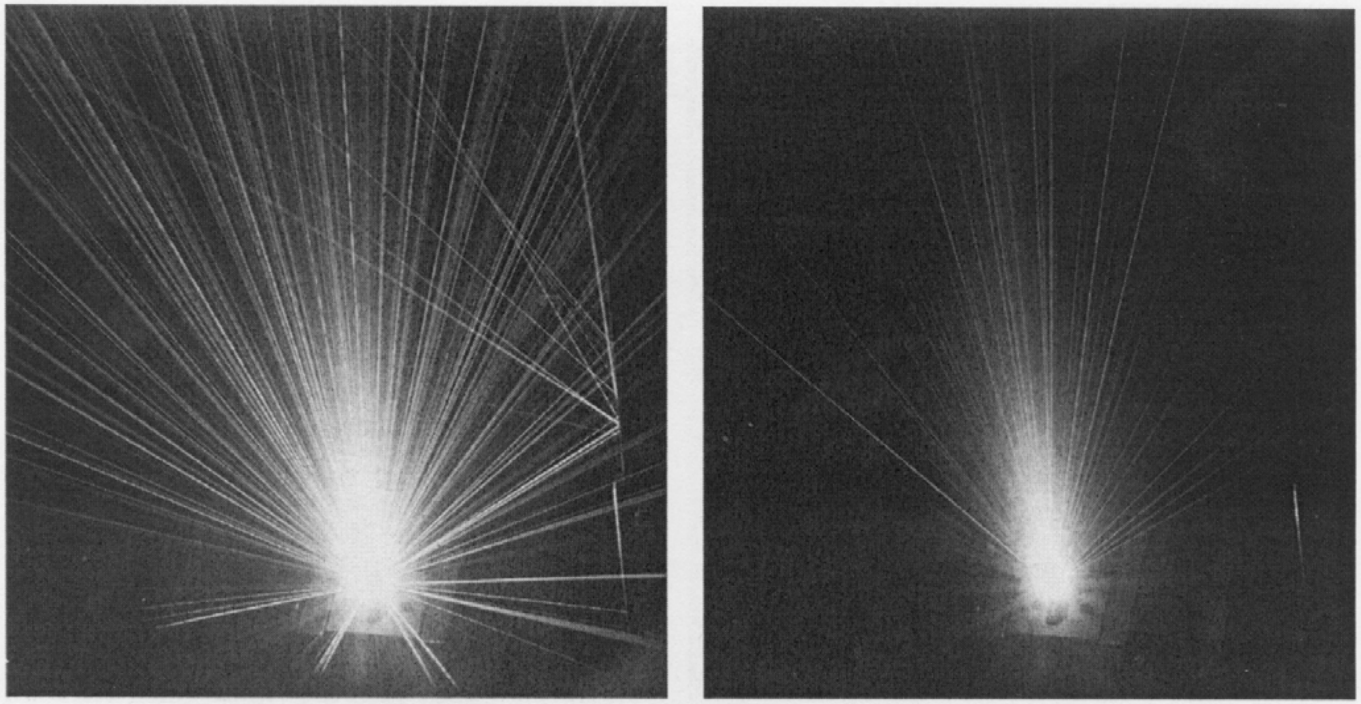

Fig. 1. Particle emission during electron beam loading of fine grain graphite (EK98) at 4.8 MJ m^{-2}, left: 1st electron beam pulse on a polished test sample, right: 5th electron beam pulse.

Cracking after thermal shock

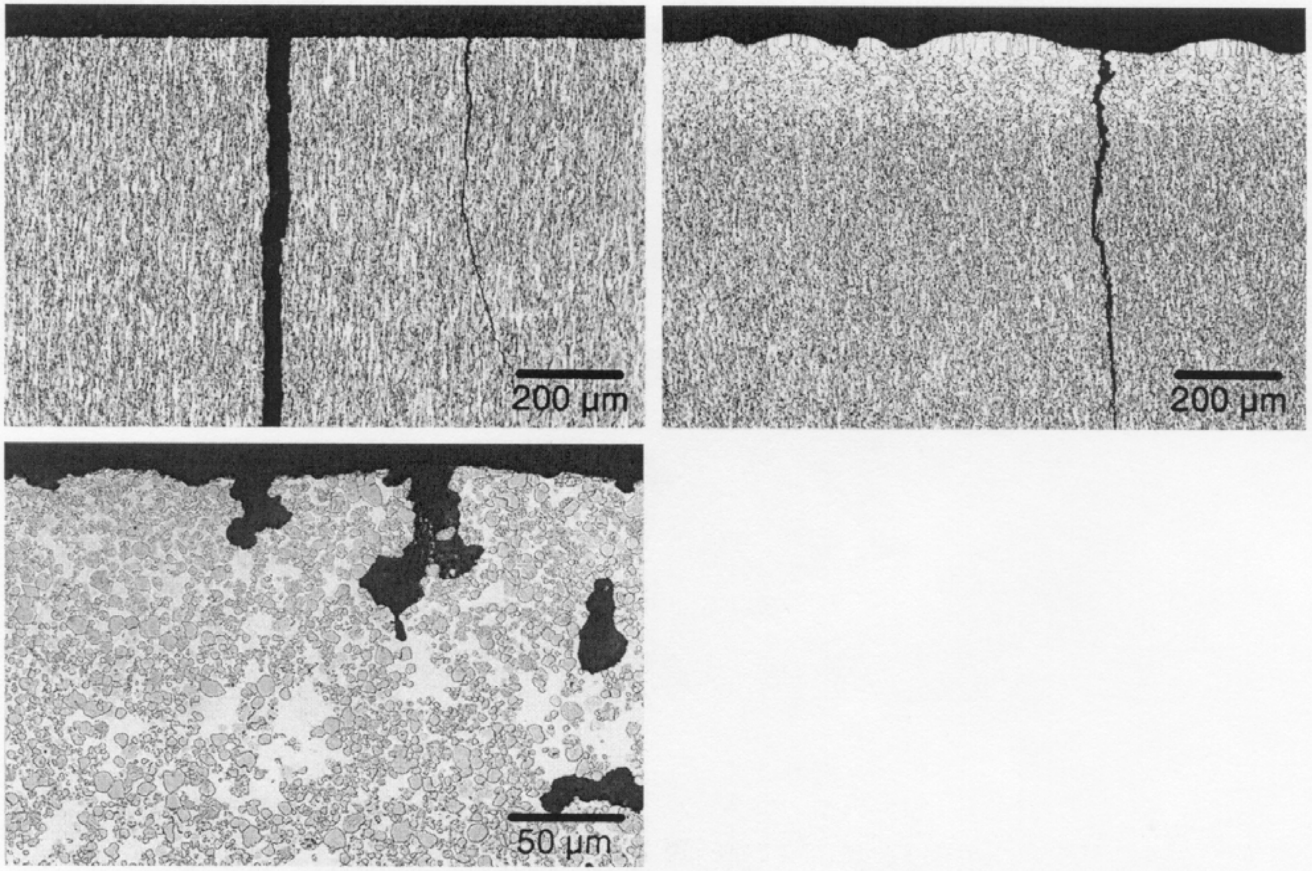

Fig. 3. Metallographic sections from different tungsten alloys loaded with five electron beam pulses ($E_{abs} = 11.8$ MJ m^{-2}, $t = 5$ ms). Left: W5Re; right: WLa_2O_3; lower left: W30Cu.

Surface Microstructure

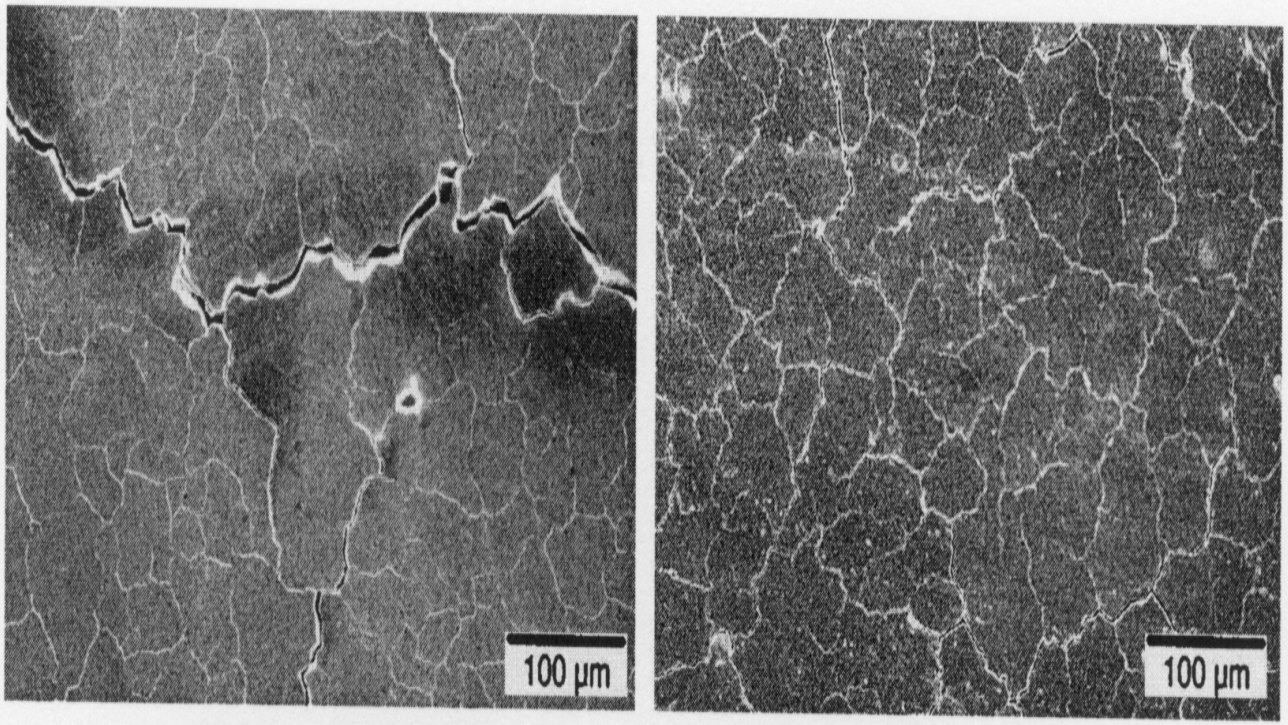

Fig. 4. Surface morphology from tungsten specimens loaded at incident energy densities of 7.5 MJ m^{-2} ($t = 360$ μs) in VIKA. Left: $T_{sample} = 330°C$, right: $T_{sample} = 640°C$.

Profiles of stopped hydrogen and helium atoms in graphite per one 7 TeV proton of LHC as a function of the depth into target and radial coordinate.

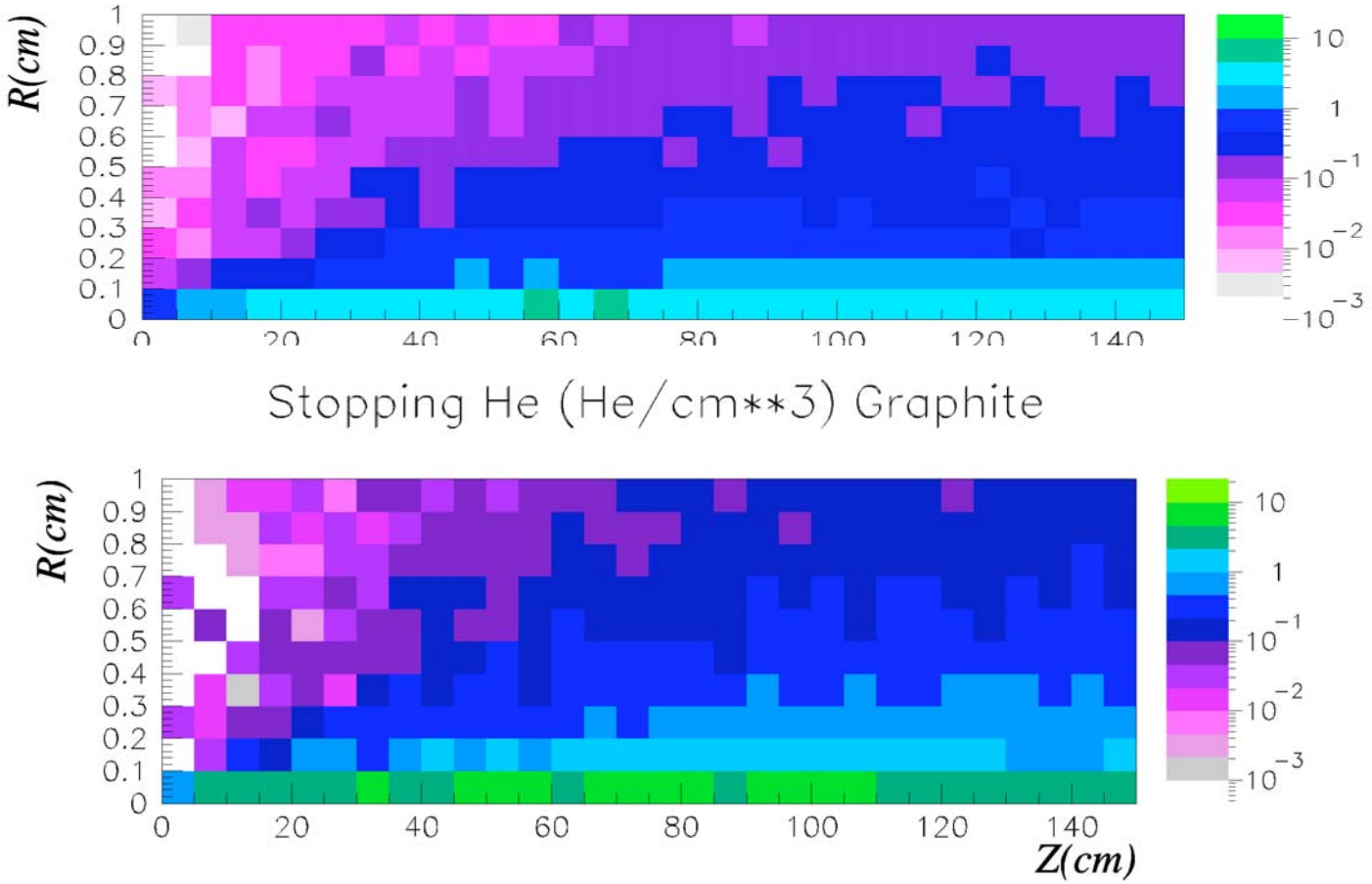

21 March, CERN, Geneva

Effect of Gas Atoms on Stability of C

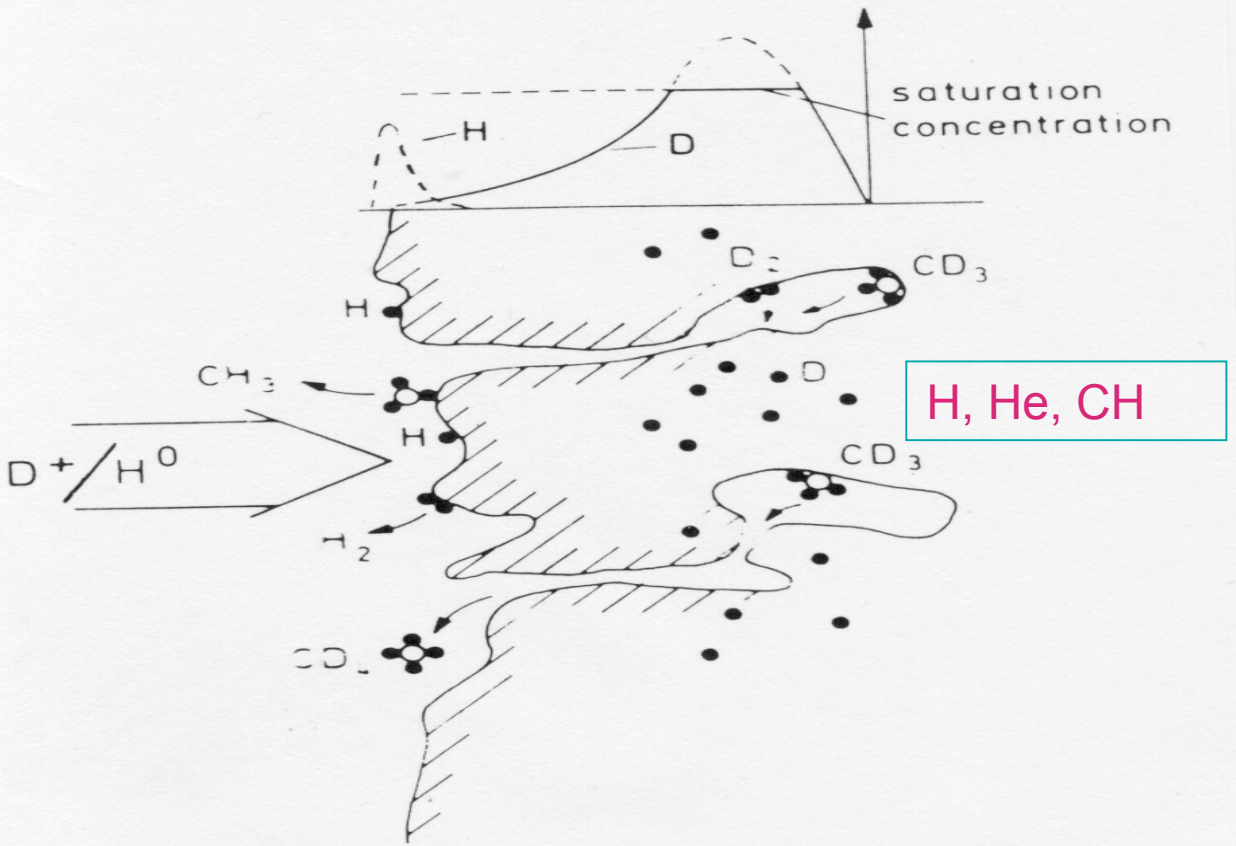

H, He, CH

Fig. 6. Schematic figure of the simultaneous bombardment of graphite with energetic deuterium ions and thermal atomic hydrogen [34,47].

Effect of H on Resistance

E. Vietzke, V. Philipps / Surface modification due to hydrogen – graphite interaction

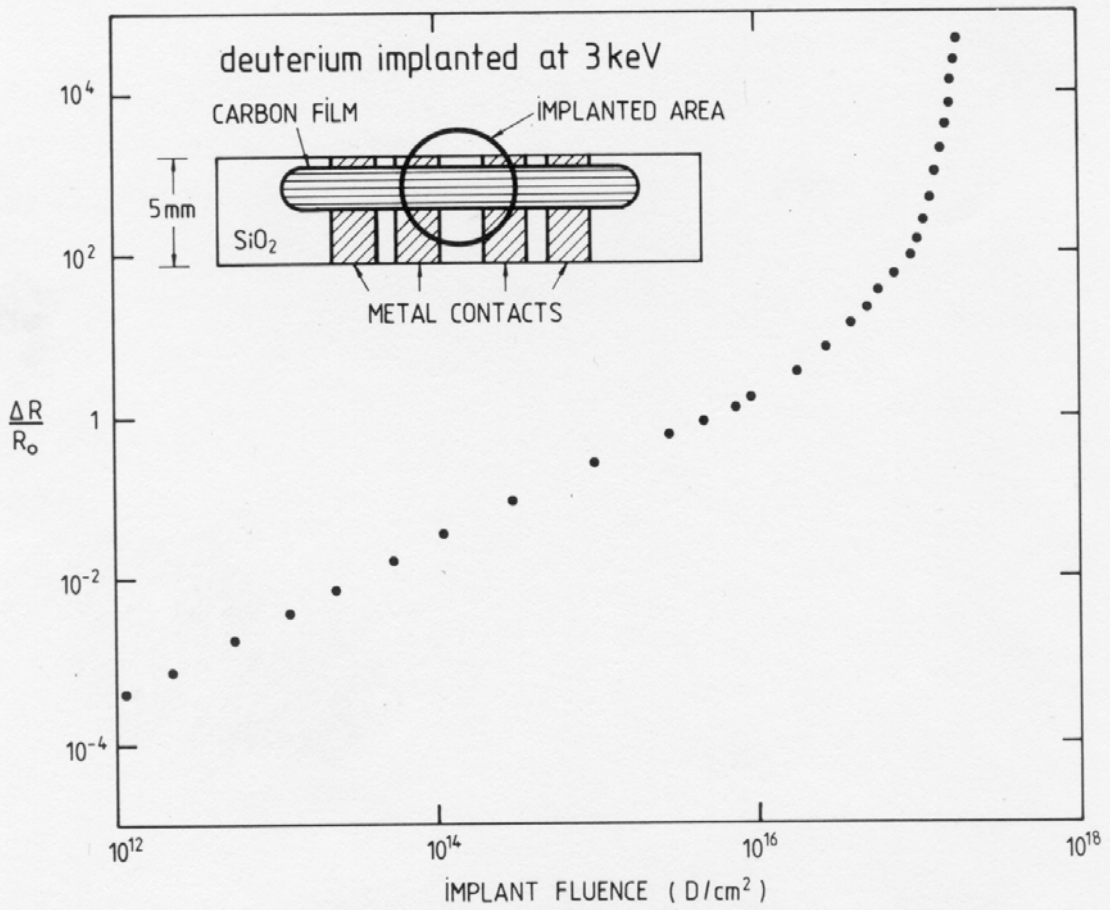

Fig. 3. Relative resistance change of a carbon film 92 nm thick vs fluence of deuterium implanted at 3 keV. At this energy the entire thickness of the carbon is being implanted [28].

Effect of Head Load on Vacuum

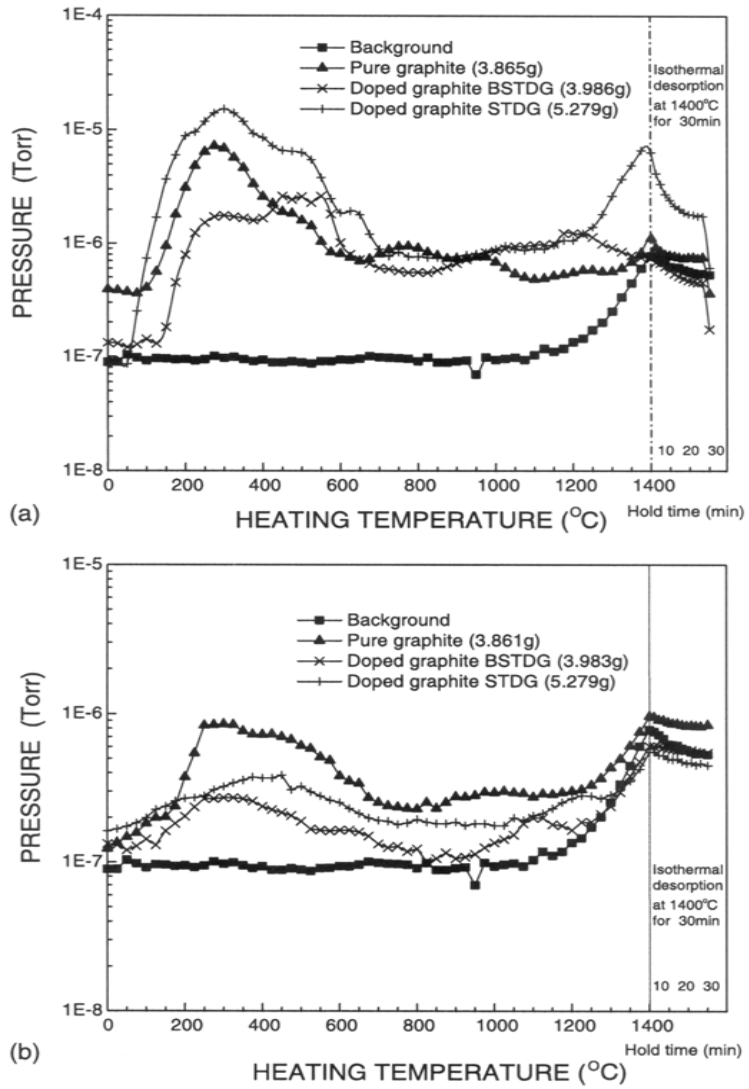

Fig. 2. TDS spectrum of carbon-based materials during (a) first heating and (b) second heating.

CO,CO2,

CH, C2HY

Effect of He on Mechanical Properties

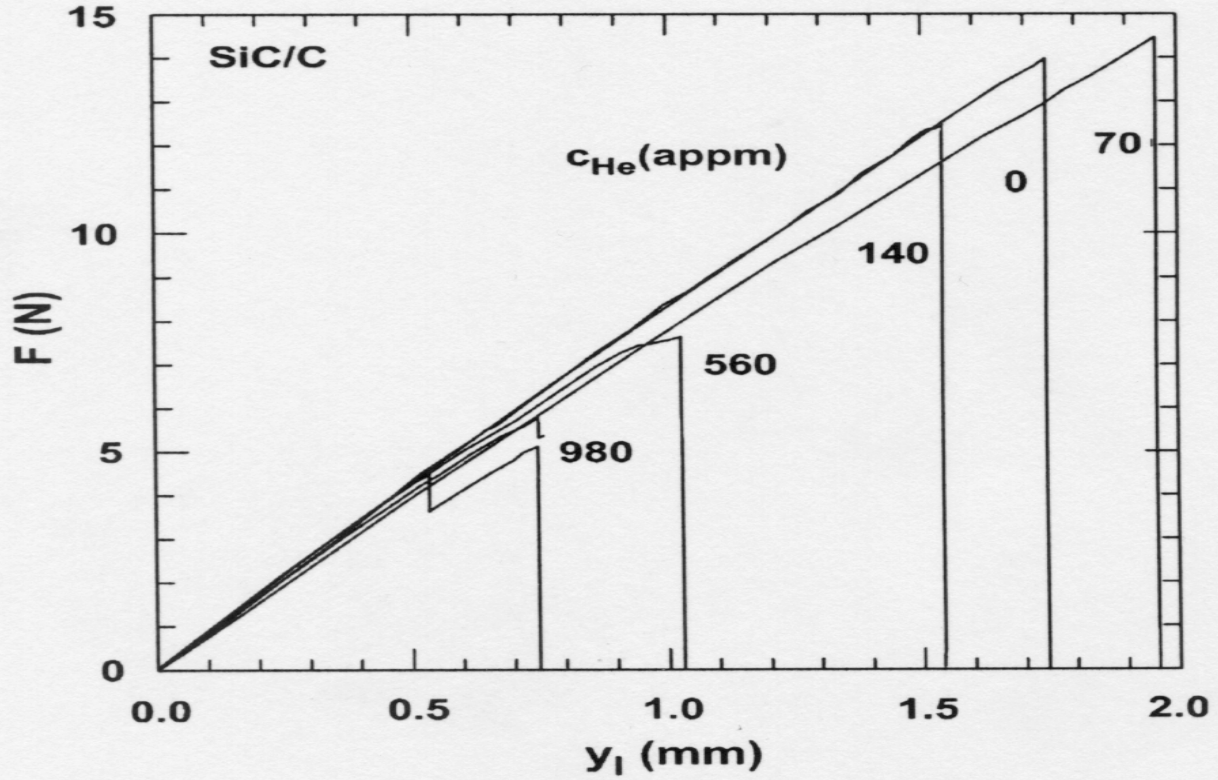

Fig. 6. Load–deflection curves of SiC/C during 3-point bending after homogeneous implantation of helium below 70 °C to a depth of 117 µm and to concentrations as indicated. The second 980 appm specimen was stopped after the first drop (crack initiation) for SEM investigation.

Effect of He on Cracking

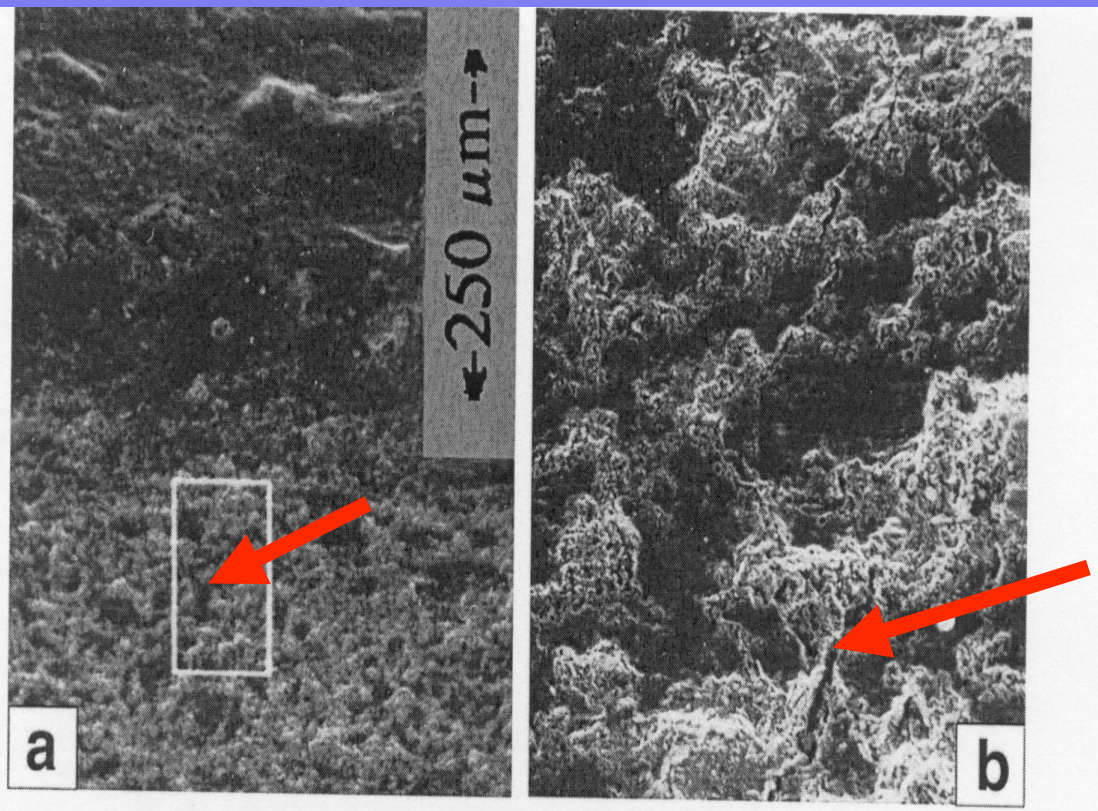

Fig. 7. Lateral view by SEM of SiC/C implanted to 700 appm He below 70 °C, showing the ≈250 μm deep implanted region (a) and an enlarged view of a crack, extending from the implanted/unimplanted interface into the unimplanted bulk (b).

Accumulation of Strain in Matrix due to Radiation Damage and He

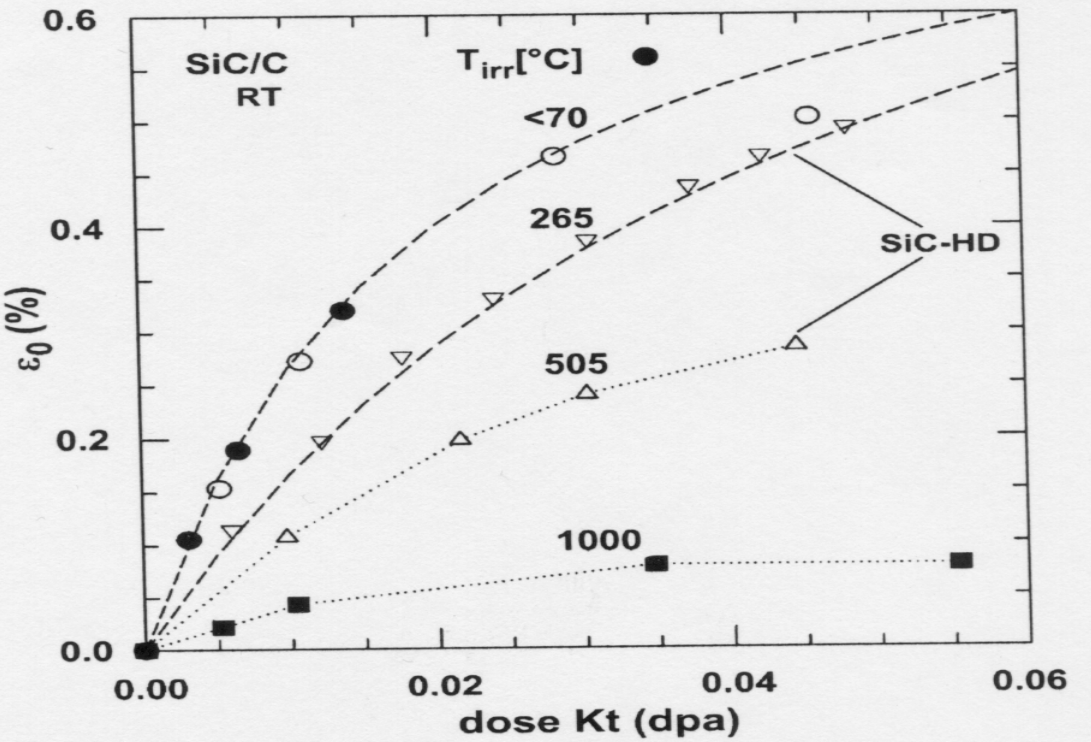

Fig. 9. Strains calculated from Eq. (6) from bending angles α (Fig. 5) for SiC/C specimens homogeneously implanted below 70 °C to depth of 117 µm (○) and 254 µm (●) and at 1000 °C to 254 µm (■), respectively. Included are strain data from SiC-HD proton-irradiated at 265 °C (▽), and 505 °C (△) without implantation [19]. The dashed lines give fits of Eq. (6); dotted lines are included to guide the eyes.

Gas filled He cavities in Graphite

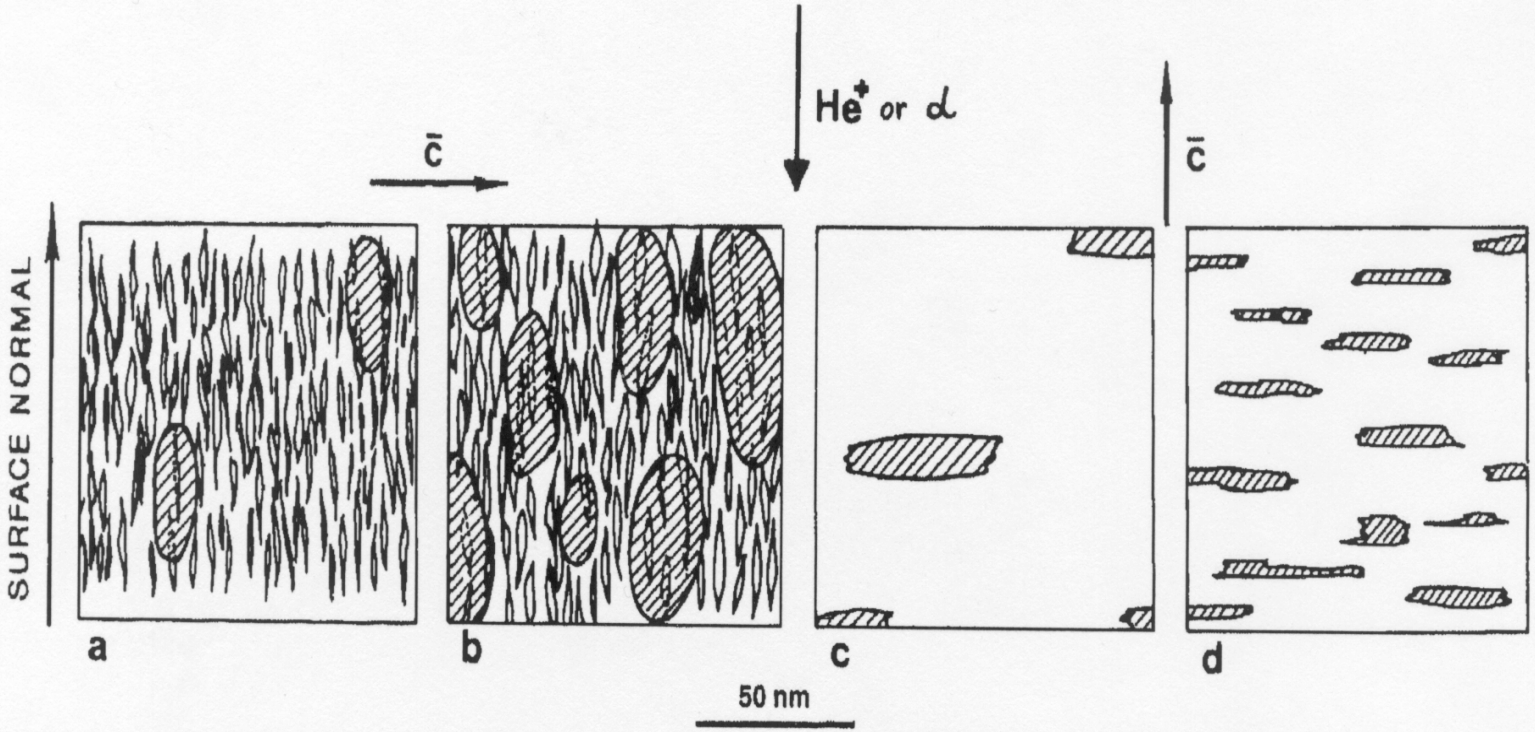

Fig. 6. Schematic presentation of He filled edge-on oriented cavities in EO PG (a,b) and BO PG (c,d) samples at a distance, $x \approx \bar{R}_P$ from the outer surface after implantation with: (a) and (c) 40 keV He ions, $\phi t_1 = 1.2 \times 10^{21}$ He m^{-2}; (b) 40 keV He ions, $\phi t_2 = 2.0 \times 10^{21}$ He m^{-2} and (d) 3.5 MeV α-particles, $\phi t = 4.3 \times 10^{21}$ α m^{-2}. All cavities except of type 1 in (a) and (b) are hatched.

He Bubbles in Graphite

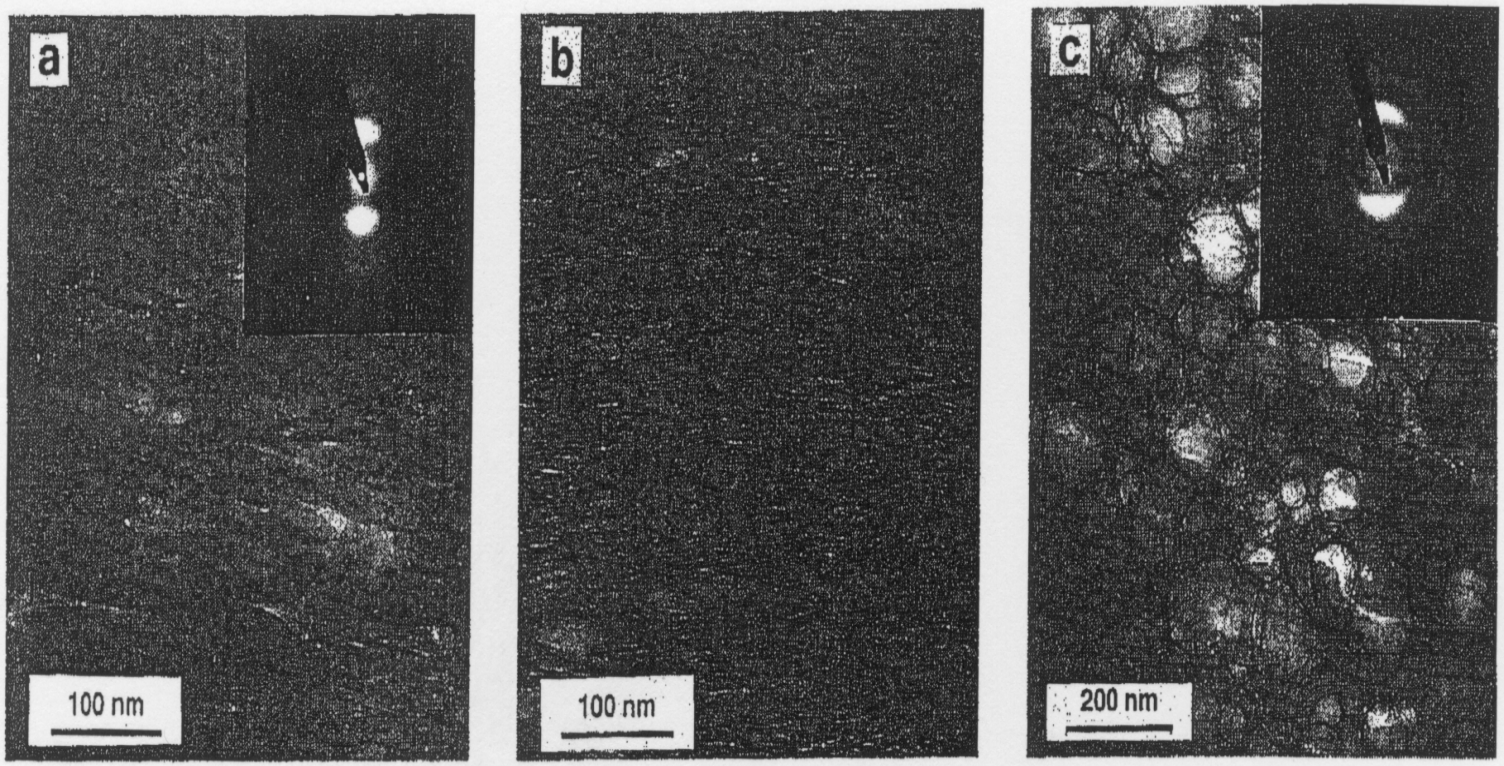

Fig. 5. Planar view of He filled cavities in EO PG implanted with 40 keV ions at RT to a fluence: (a) 1.2×10^{21} He m^{-2}; (b) 2.0×10^{21} He $^{-2}$; (c) 5.0×10^{21} He m^{-2} [5]. Note micrograph scales! Corresponding SADPs are on inserts.

Cracking In Graphite with He

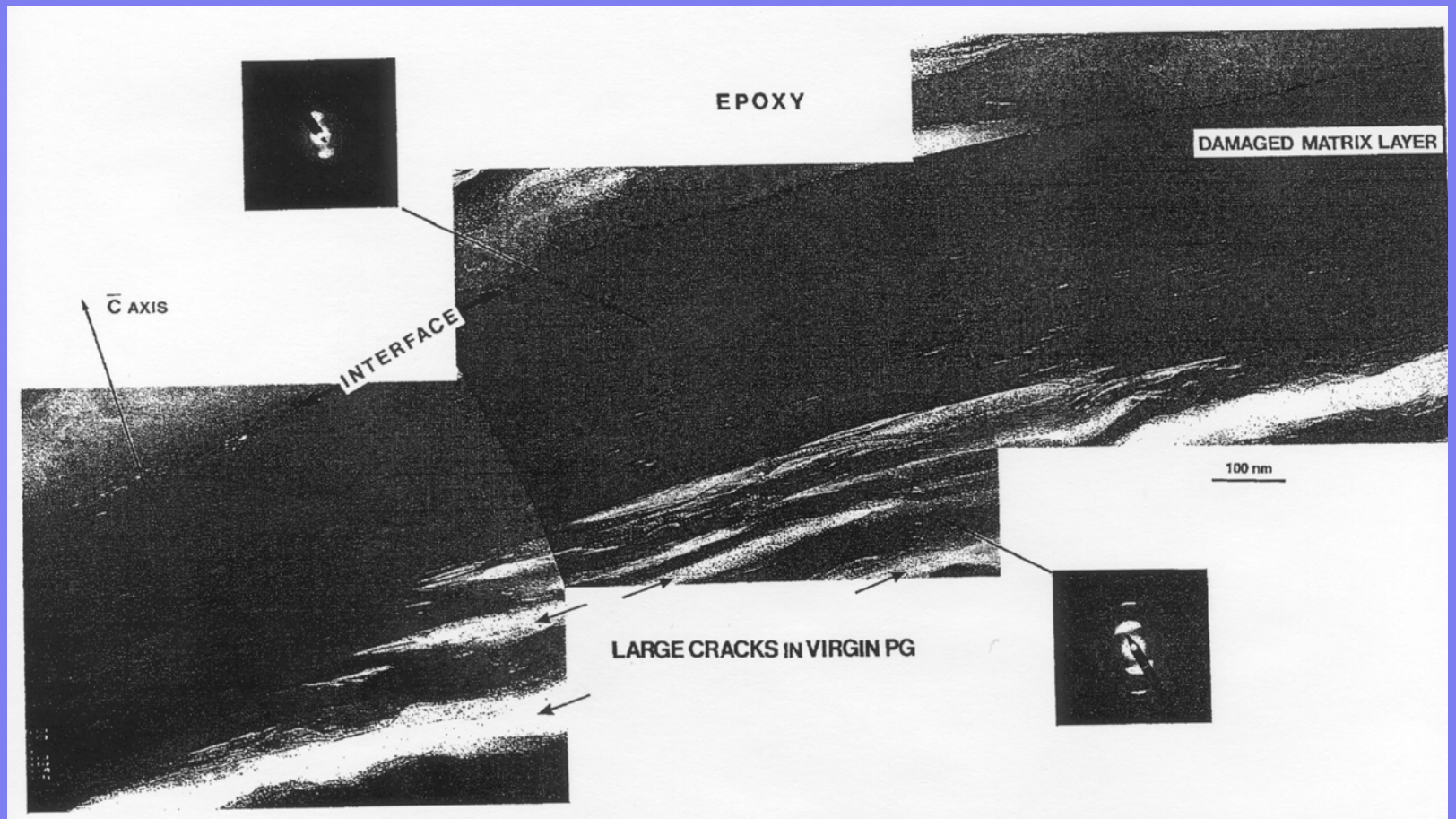

. 8. Cross sectional view of the microstructure of BO PG sample implanted with 40 keV He ions at RT up to a fluence $\phi t_1 = 1.2 \times 10^{21}$ He m^{-2}. SADPs on top a
tom refer to the damaged layer and to the underlying matrix, respectively.

Surface Erosion in Graphite due to He

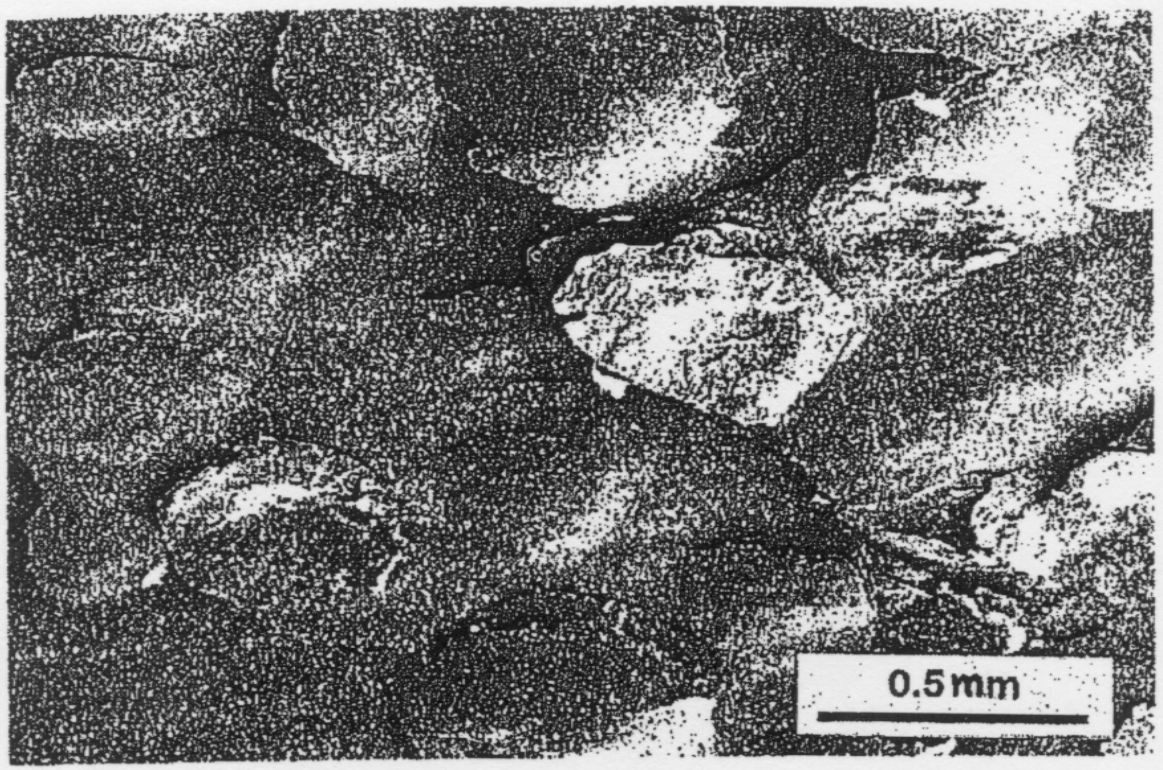

Fig. 11. SEM micrograph of blisters on the surface of BO PG implanted with 3.5 MeV He ions at 770 K to a helium peak concentration of 5.6 at%.

Elastic Modulus Change due to Radiation Damage

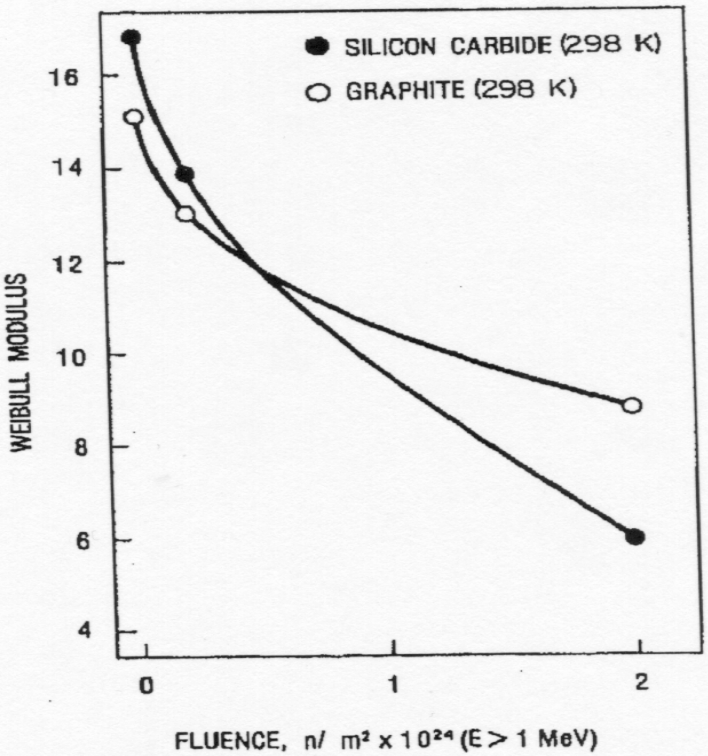

Fig. 3. Weibull modulus vs. neutron fluence for graphite and silicon carbide at room temperature.

Radiation Swelling in Graphite under Neutron Irradiation

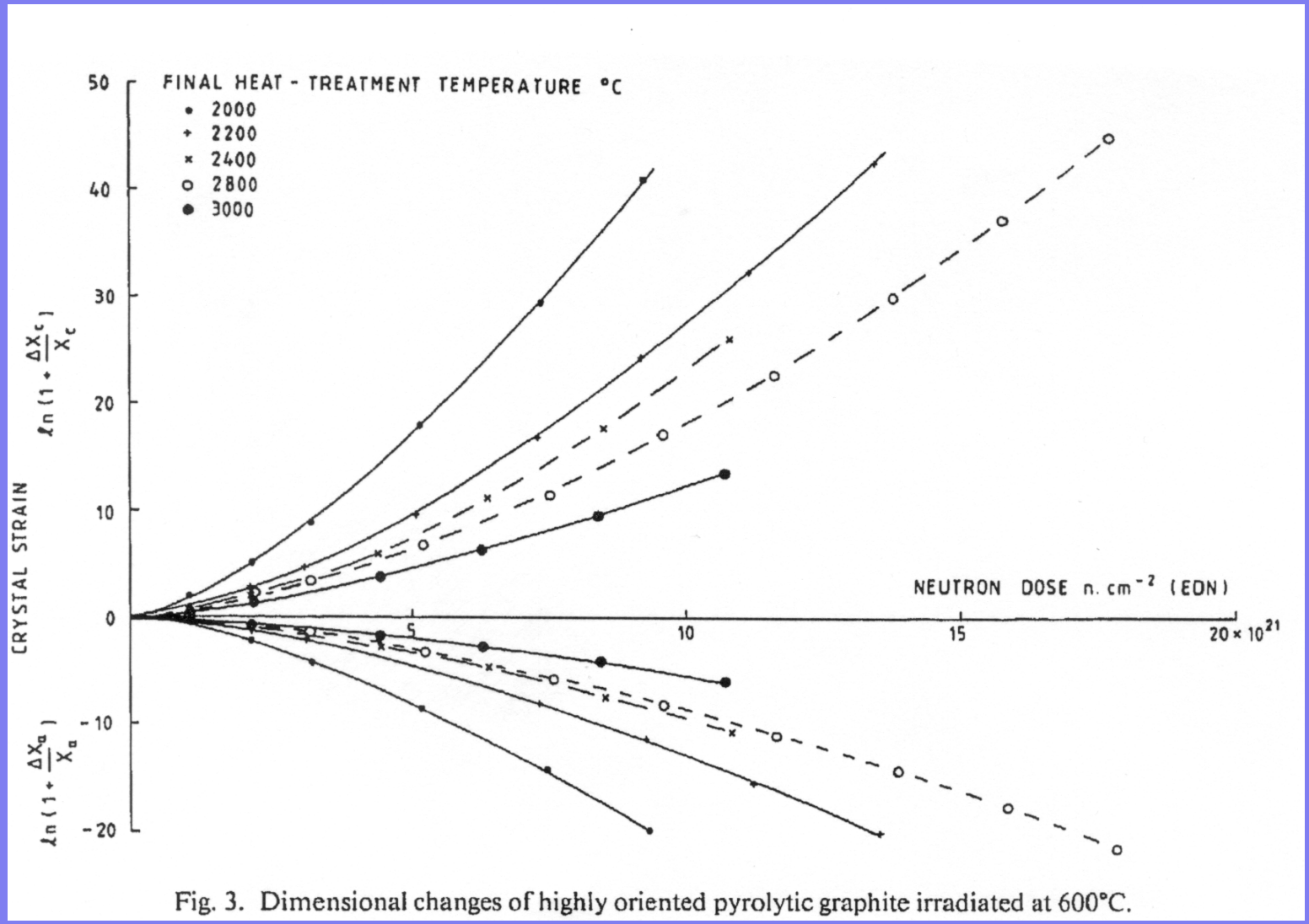

Fig. 3. Dimensional changes of highly oriented pyrolytic graphite irradiated at 600°C.

Radiation Swelling in Graphite under Neutron Irradiation

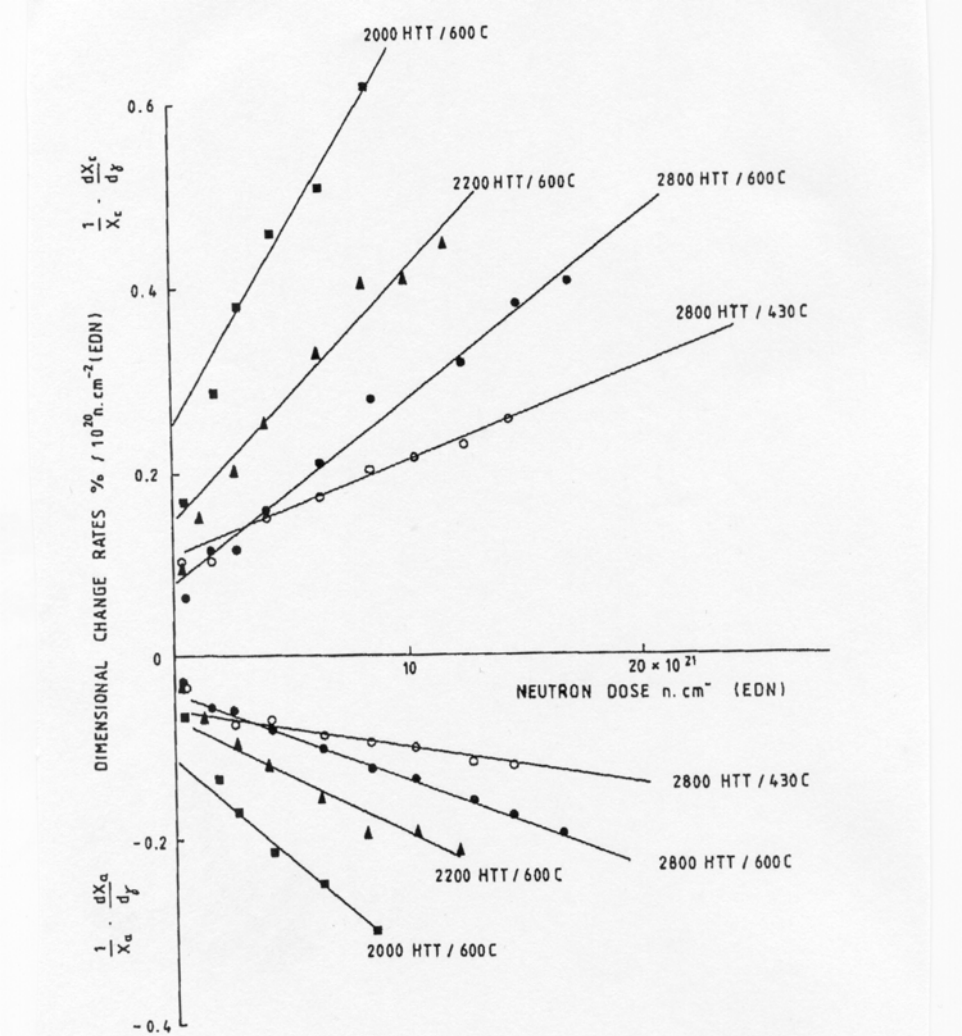

Fig. 5. Selected comparisons of dimensional change rates with $a_1 + 2a_2\gamma$.

21 March, CERN, Geneva

Mechanical Properties Change in Graphite under Neutron Irradiation

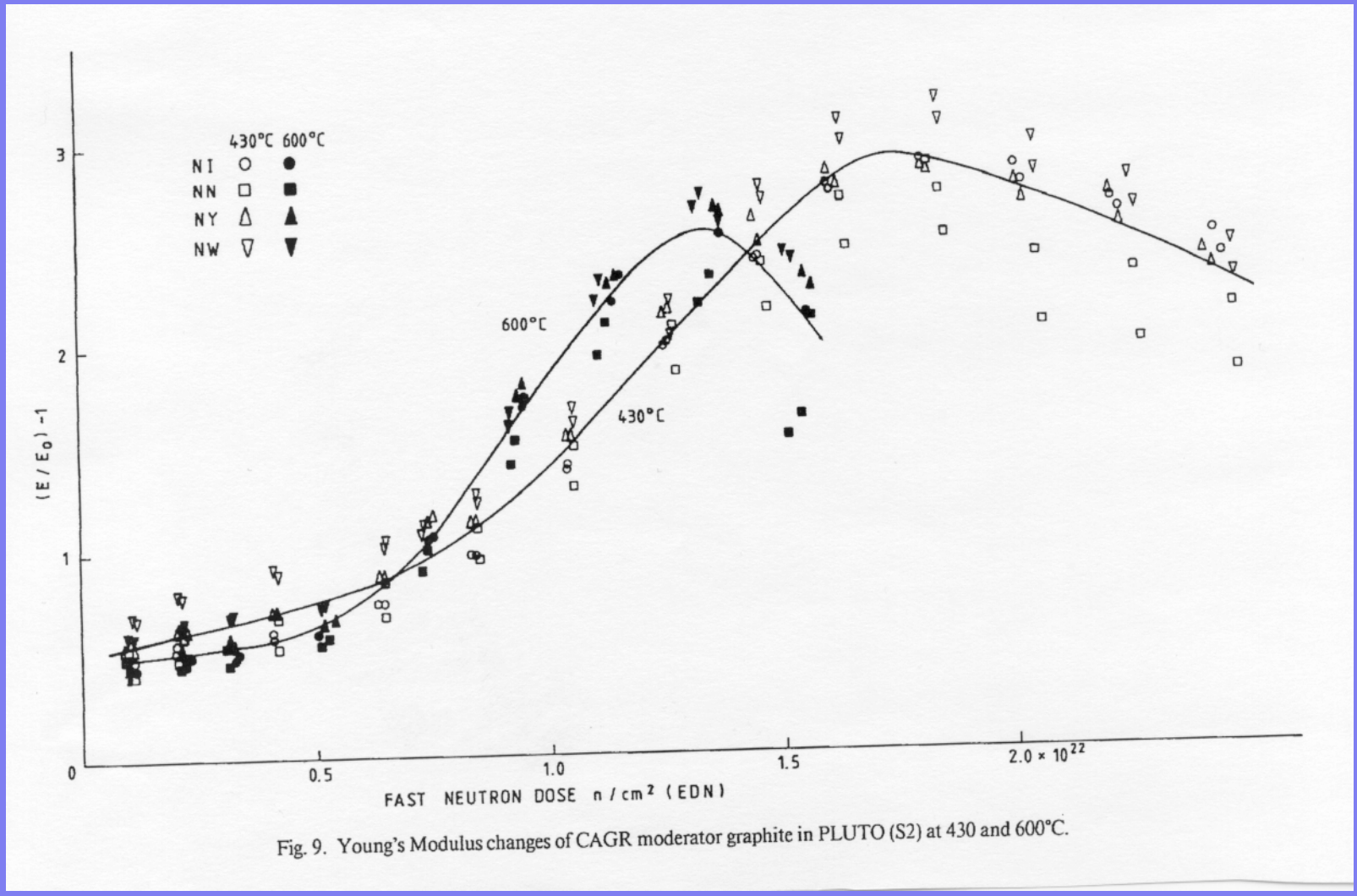

Fig. 9. Young's Modulus changes of CAGR moderator graphite in PLUTO (S2) at 430 and 600°C.

21 March, CERN, Geneva

Initial Microstructure of Graphite

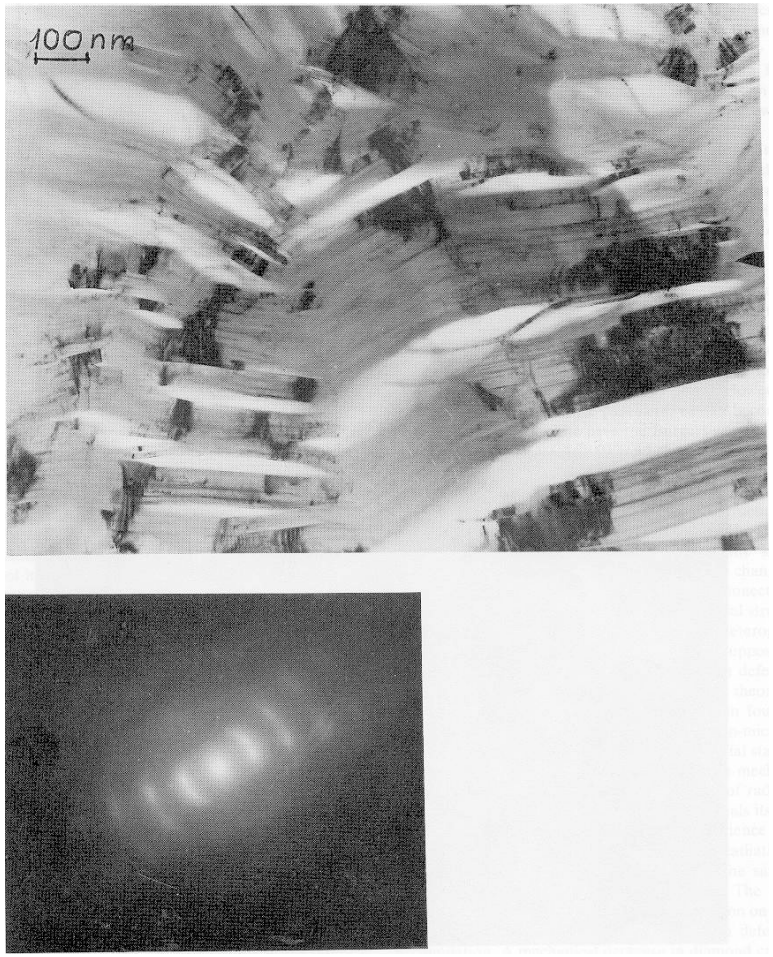

21 March, CERN, Geneva

Radiation Damage Formation: Interstitials and Vacancy Dislocation Loops in Graphite under Neutron Irradiation

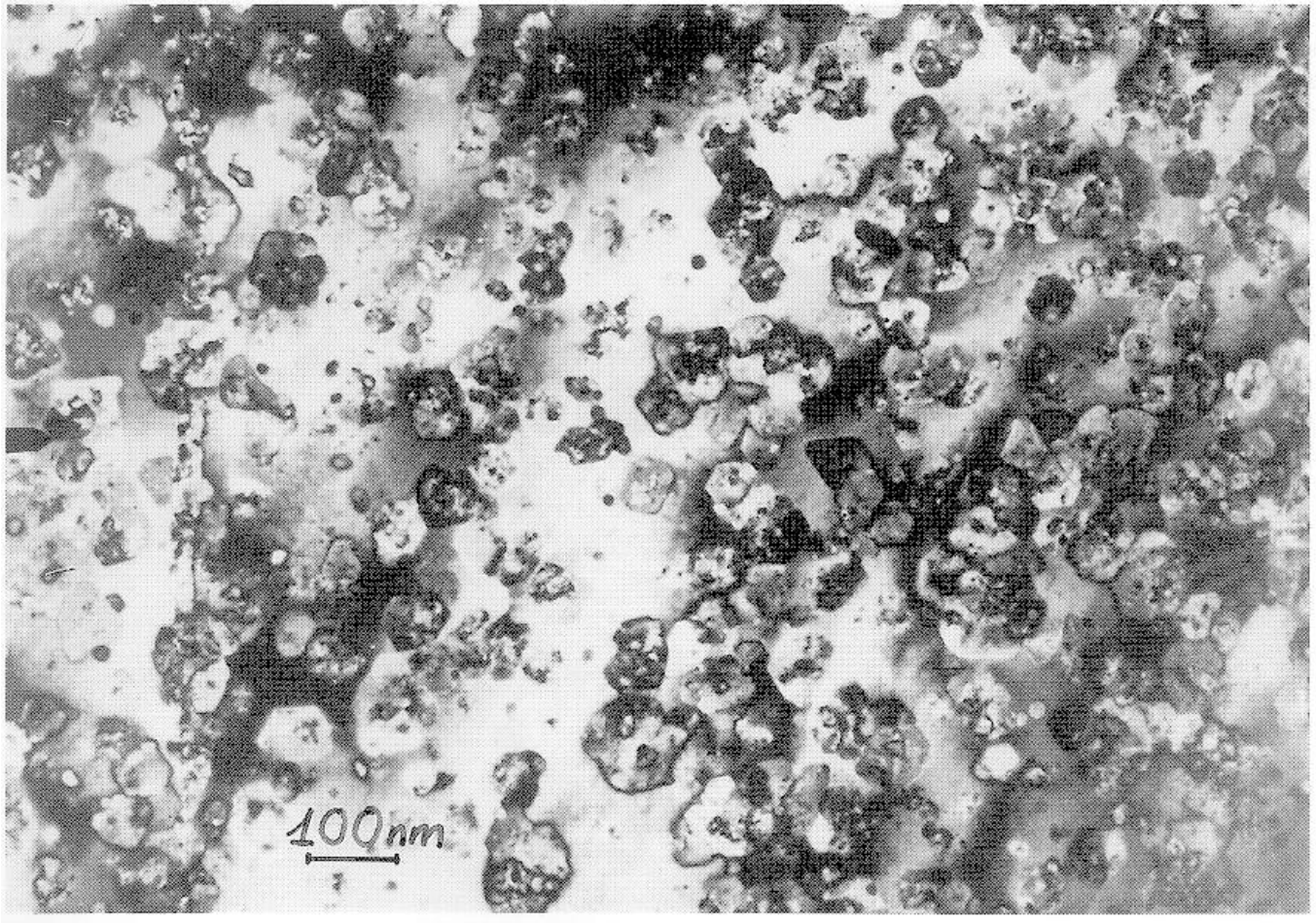

21 March, CERN, Geneva

Tests of Graphite in RRC KI

- Measurements of temperature dependencies of thermal conductivity in graphite from T = 20 – 750 C near and far from proton beam
- Measurements of temperature dependencies of electrical conductivity in graphite from T = 20 – 750 C near and far from proton beam
- Measurements of mechanical properties: elastic modulus in the temperature interval T = 20 – 750 C near and far from proton beam
- Measurements of mechanical properties: deformation curves before rupture near and far from proton beam
- Transmission and Scanning Electron Microscopy of initial microstructure and microstructure change near and far from proton beam in the temperature interval T = 20 – 750 C